INFN/AExxx, LAL-xxx, SLAC-R-xxx

Super$B$ Detector Technical Design Report

Abstract

This report describes the technical design detector for Super$B$.

Contents

9 Electromagnetic Calorimeter

9.1 Overview

Calorimetry at Super$B$ is achieved with three major components: A CsI(Tl) "barrel" calorimeter covering the central region, a LYSO(Ce) "forward" calorimeter covering the small angle region in the direction of the high energy beam, and a lead-scintillator "backward" calorimeter covering the small angle region in the direction of the low energy beam. Table 9.1 shows the solid angle coverage for each of the three parts of the SuperB EMC. The superB electromagnetic calorimeter (EMC) will play an essential role in the study of the flavor physics especially in the sector in which B meson decays involve neutral particles. The calorimeter provides energy and direction measurement of photons and electrons, reconstruction of neutral hadrons such as π^0's and discrimination between electrons and charged hadrons. Many channels containing missing energy due to the presence of neutrinos will rely on information from the EMC to discriminate against backgrounds.

The SuperB EMC reuses the barrel part of the BaBar EMC detector consisting of 5760 CsI(Tl) crystals as shown in Fig. **??**. However the *BABAR* forward calorimeter will need to be replaced, due to the higher radiation and higher rates at SuperB compared with PEP-II. The forward endcap will be replaced by a new scintillating crystal calorimeter designed to work well in this new environment. Compared with the BaBar calorimeter where good energy and position resolution are required, the same criteria apply for SuperB. After an intensive R&D program the baseline option for the SuperB forward calorimeter is to use the faster and more radiation resistant LYSO crystals. As will be discussed below, this is the clear favorite in terms of performance and radiation hardness over the alternatives we have considered. The faster response time and shorter Moliére radius serve together to address the higher event and background rates. LYSO is a fast scintillator largely used in medical applications with crystals of small size. The R&D was concentrated on the optimization of performance for large crystals (2cm x 2 cm x 20 cm) with good light yield uniformity and optimized Ce doping in order to have the best possible light output. Thanks to this effort, more than one producer is able to grow LYSO crystals of good quality that can be used in high energy physics applications. Table **??** shows the comparison between LYSO and other materials used in electromagnetic calorimeters. The largest disadvantage of LYSO is cost, and we have studied lower cost alternatives as described below.

Finally, a lead-scintillator-sandwich backward endcap calorimeter improves the hermeticity of the detector. The main purpose of this component is to detect energy in the bacward endcap region, as a veto of with extra "extra" energy. This is particularly important for studying channels with neutrinos in the final state. Because of the fast time response, the backward EMC may also have a role in particle identification by providing time-of-flight for the relatively slow backward-going charged particles.

9.1.1 Background and radiation issues

One of the major concerns for the electromagnetic calorimeter is its capability to sustain the radiation dose, dose which is larger than in previous experiments due to the increased luminosity. The dominant contribution to radiation in SuperB is in fact expected to come from radiative bhabha events, that emit a large number of low energy photons at an extremely high rate. This photon rate can impact the performances

Table 9.1: Solid angle coverage of the electromagnetic calorimeters. Values are obtained assuming the barrel calorimeter is in the same location with respect to the collision point as for *BABAR*. The CM numbers are for massless particles and nominal 4 on 7 GeV beam energies. The barrel Super*B* row includes one additional ring of crystals over *BABAR*.

Calorimeter	$\cos\theta$ (lab)		$\cos\theta$ (CM)		Ω (CM)(%)
	minimum	maximum	minimum	maximum	
Backward	-0.974	-0.869	-0.985	-0.922	3.1
Barrel (*BABAR*)	-0.786	0.893	-0.870	0.824	84.7
Barrel (Super*B*)	-0.805	0.893	-0.882	0.824	85.2
Forward	0.896	0.965	0.829	0.941	5.6

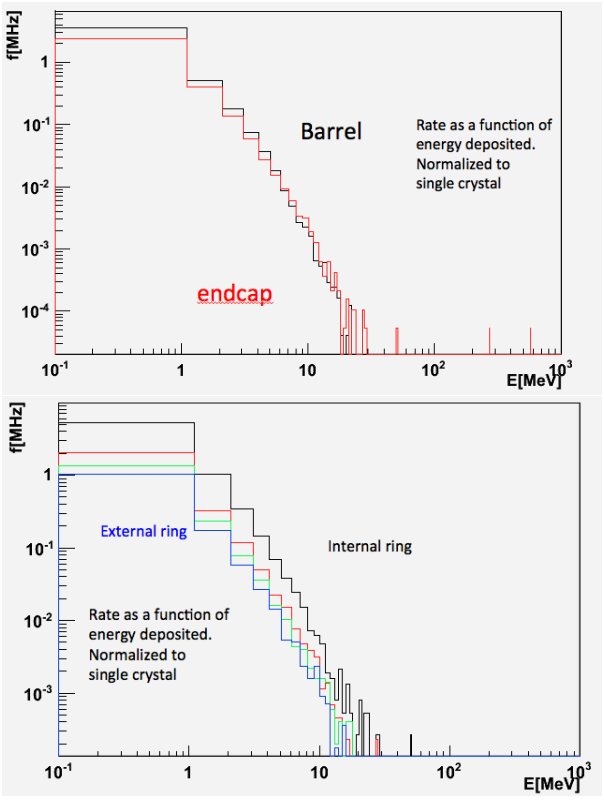

Figure 9.1: Machine Background rates per crystal as a function of deposited energy.

of the detector because of two effects: the radiation can reduce the transmittance of the crystals and therefore alter as a function of time the calibration of the detector; the large number of photons can pile-up with the other effects thus introducing a degradation in energy resolution.

To estimate the impact of these effect a full simulation has been setup as described in Sec.**WHICH SECTION?**. The simulation outputs the energy deposited by radiative Bhabha events in the individual crystals at each beam crossing. i.e. every 2.1ns. This can be converted in terms of rate of photons of a given energy impacting each crystal. The result is shown in Fig. 9.1, both (left) averaging over the whole Barrel and the whole FWD and (right) averaging over the rings of the FWD which have the same number of crystals per ring. The result shows that there is no significant difference in the irradiation between the Barrel and the Endcap. This can be understood because the dimension of the crystals is significantly different: due the different density and consequently molier radius, the transverse dimensions of LYSO or BGO crystals are two times smaller than the CsI crystals (both doped and not) and the overall volume of a LYSO or BGO crystal is 6.7 times smaller (120cm^3 vs 800cm^3) than the CsI ones. Since the rates of signals from the machine background scales linearly with volume, the most forward crystals of the Barrel will suffer a background more than six times larger than the more central crystals of the FWD calorimeter, albeit contiguous.

On average therefore each crystal (both of Barrel or Endcap) will see 1MHz of photons between 1 and 5 MeV and 10 KHz of photons between 5-10 MeV. A plausible linear extrapolation in log-log scale would lead to 100Hz between 10-50 MeV and 1Hz between 50-100 MeV.

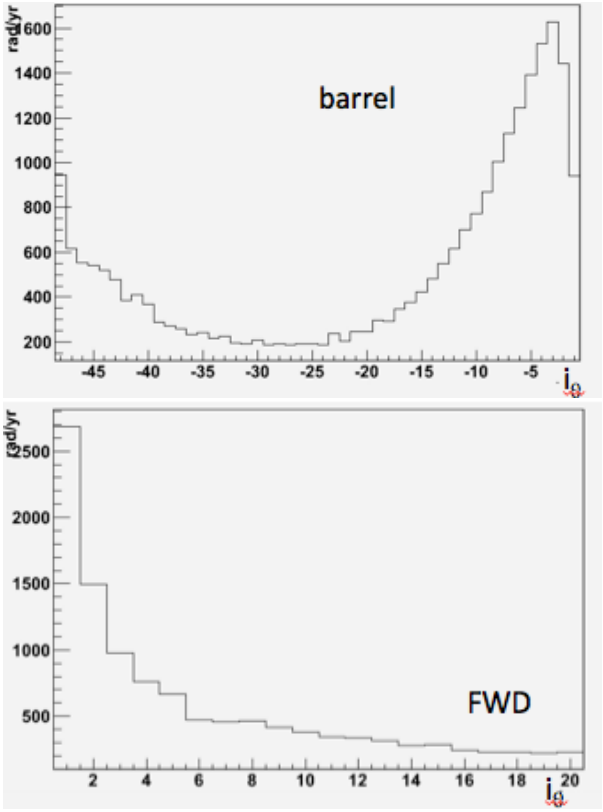

Figure 9.3: Integrated dose as a function of i_θ for the Barrel (Left) and FWD (Right) EMC.

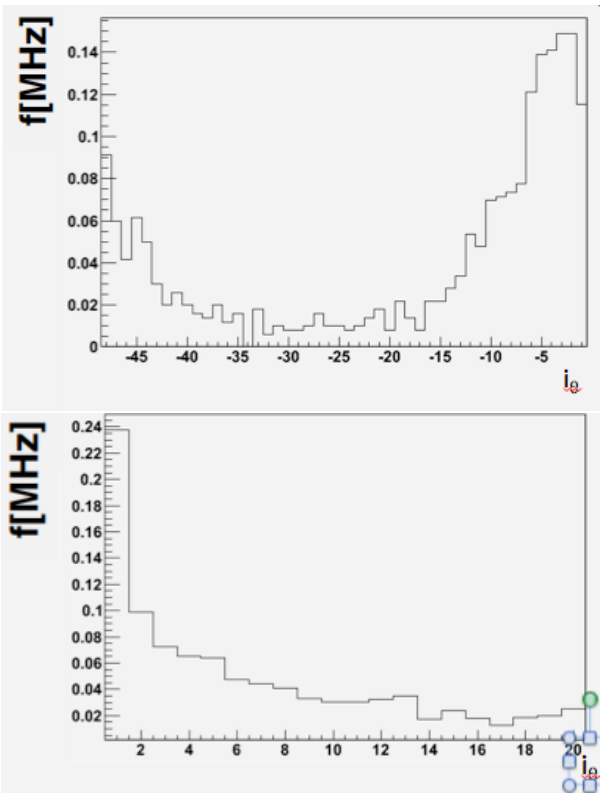

Figure 9.2: Integrated rates for $E > 5$MeV as a function of $i_\theta$for the Barrel (Left) and FWD (Right) EMC.

The ring-by-ring details are shown in Fig. 9.2, where the integrated rate of deposits larger than 5MeV are estimated as a function of an index, i_θ which is $i_\theta < -49$ for the backward calorimeter, $-49 =< i_\theta < 0$ for the barrel ($i_\theta = -1$ corresponding to the most forward ring), and $i_\theta > 0$ for the FWD EMC ($i_\theta = 1$ corresponding to the innermost ring) . It can be noted that the forward region of the barrel ($i_\theta > -10$) is more irradiated than the FWD calorimeter, a part from the innermost ring which is a factor two worse than any other ring.

From the radiation hardness point of view, the dose to which the crystals are sensitive is defined as the total energy deposited in a crystal divided by its mass. The dose expected per year (conventionally considered $10^7 s$ long) and per crystal is shown in Fig 9.3 separately for the Barrel and the FWD. Conservatively, assuming a maximum of 10 years of operations, crystals need to be radiation resistent up to at least 30krad. Also the impact on resolution of a $\sim$ 1rad/hour dose rate needs to be considered.

9.1.2 Simulation tools

9.1.2.1 Fastsim

9.1.2.2 Full sim

9.2 Barrel Calorimeter

We propose to re-use the barrel portion of the *BABAR* EMC, retaining the fundamental mechanical structures and the 5760 CsI(Tl) crystals and associated pairs of photodiodes mounted on each crystal, along with some modifications required for optimal performance at Super$B$.

Below, we describe first the condition, as of the end of Babar running, of the CsI(Tl) crystals which will be reused in the SuperB detector. We then discuss the additional factors present at SuperB, principally the high pile-up and backgrounds environment, which must be addressed to optimize energy resolution. We then describe the mechanical design and calibration systems for the barrel, each of which will be minimally changed from their current configurations, as well as the detector readout. We next discuss the barrel's energy and position resolution, as well as the $\gamma\gamma$ mass resolution, and the effects on these due to long-term exposure to backgrounds at Babar. These trends are extrapolated to decreases in performance which might be expected over the lifetime of SuperB.

We then describe the current barrel crystal photodiodes, which will be reused for SuperB and not replaced, and the changes proposed for the on-crystal pre-amplifier package and the front-end electronics. Lastly, we present the proposed plan for the de-integration of the barrel EMC down to its component mechanical structures and carbon-fiber modules, the packaging and shipping of the various parts and structures, and their local storage at a facility at or near Tor Vergata.

9.2.1 Requirements Relevant to the SuperB Environment

9.2.1.1 Crystal Aging at BABAR

Over the span of Babar's running, the EMC barrel crystals have been damaged to a certain extent by high levels of radiation, which was monitored by 116 radFETs distributed throughout the subdetector. The most common form of damage [1] comes from the development of absorption bands which reduce an affected crystal's light yield. Although crystals in the EMC endcap experienced higher levels of radiation than those in the barrel, all EMC crystals from the furthest backward to those more forward integrated non-negligible doses. The resulting changes in crystal light yields were monitored and corrected for during Babar operation using calibrations performed at either end of the dynamic range of the detector: a low-energy calibration using a 6.13 MeV radioactive photon source, which is discussed below in Sec. **??**, and a high-energy calibration with Bhabha events.

The change in light yield for barrel crystals as a function of absorbed radiation dose, based on the low-energy calibration data, is shown categorized by crystal manufacturer in Figure 9.4. Though care was initially taken to produce uniformity between crystals before they were integrated into the detector, there have been varying degrees of degradation in performance as time has progressed. Depending on the manufacturer, the total decrease in light yield can be up to $\sim 10\%$. Much of the decrease in light yield occurred during the initial years of Babar running and, as the integrated dose increased, there was less light loss per unit dose received. However, as can be seen in Fig. 9.4, in the SuperB environment, the eventual loss in light yield for the worst-performing barrel crystals, generally those provided by Kharkov and Hilger, may be substantial. The relative poor performance of the crystals provided by these manufacturers was known at the time of the barrel's construction and, to the extent possible, these manufacturers' crystals were placed as far backwards in polar angle as possible. as is shown in Fig. 9.4.

9.2.1.2 Backgrounds

In addition to crystal aging, background can degrade energy resolution due to electronic signal pile-up. The dominated source is expected to be photons and neutrons from radiative Bhabha events interacting with the detector material. This effect is negligible in *BABAR*. But in Super*B*, it could be substantial, especially in the low energy range.

The pile-up effect is a function of signal pulse shape. Since Super*B* is reusing *BABAR*'s barrel, the long decay time of CsI(Tl) crystal cannot be changed. Nonetheless, readout and electronics can be optimized to minimize the the impact of the pile-up effect. To ensure similar physics sensitivity as *BABAR*, the background pile-up should have a negligible effect in energy resolution of high energy photons (*how high?*)

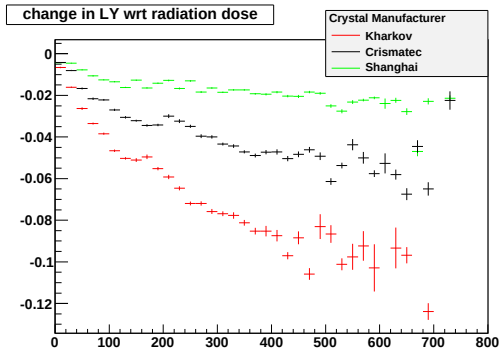

(a) Barrel backward

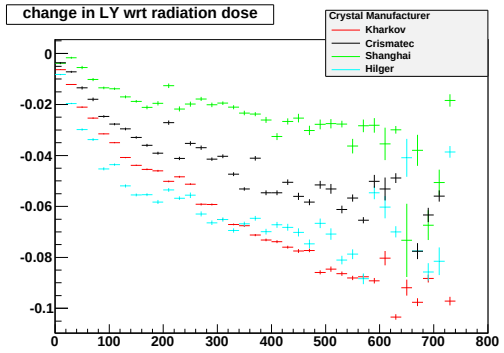

(b) Barrel forward

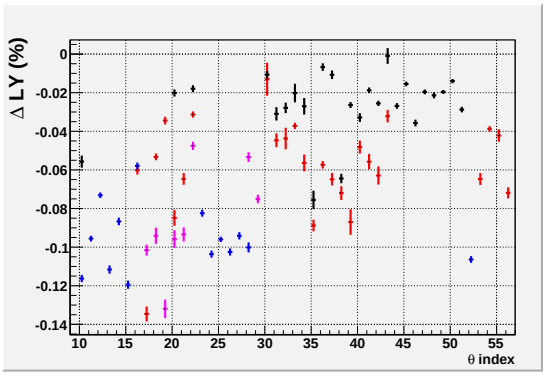

(c) Δ LY vs theta

Figure 9.4: Backward and forward barrel crystal light yield decreases for plotted with respect to absorbed radiation dose, with the different crystal providers indicated. The bottom plot shows the light yield decrease as a function of polar angle index for each manufacturer using the same color legend.

and contribute to no more than $x\%$ to energy resolution of photons at 100 MeV.

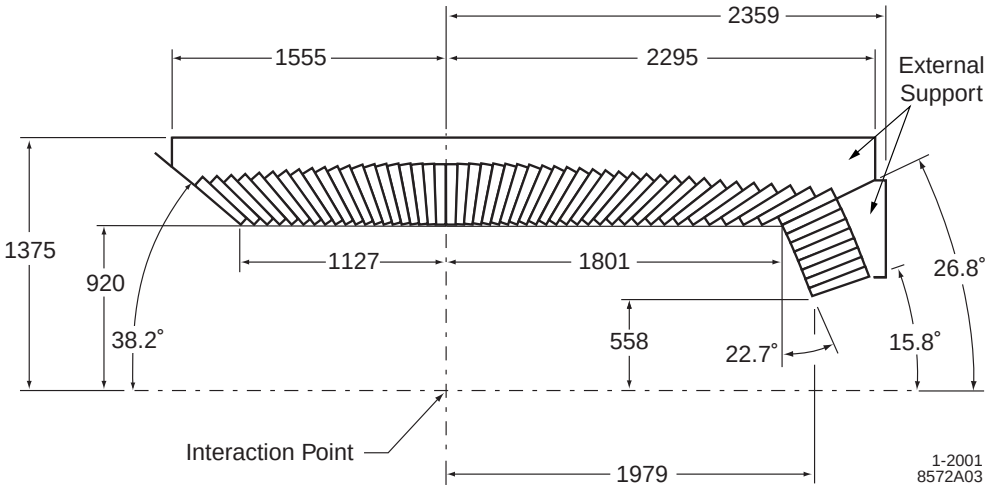

Figure 9.5: Longitudinal EMC cross-section (only the top half is shown) indicating the arrangement of the 48 barrel and 8 endcap crystal rings. The detector is axially symmetric around the z-axis. All dimensions are in mm.

9.2.2 Description of BABAR Barrel Calorimeter

9.2.2.1 Mechanical design

The Babar barrel EMC consists of a cylindrical barrel with full azimuthal coverage, extending in polar angle from 26.8° to 141.8°. A longitudinal cross-section, including the forward endcap, is shown in Figure 9.5. The barrel EMC contains 5,760 crystals arranged in 48 separate azimuthal rings, with 120 identically dimensioned crystals in each ring. Each crystal has a tapered trapezoidal cross section, with length increasing from 29.6 cm furthest backward to 32.4 cm furthest forward in order to minimize the effects of shower leakage from increasingly higher energy particles. To minimize the probability of preshowers, the crystals are completely supported at the outer radius, with only a thin gas seal at the front. The amount of material in front of the crystal faces is $0.3 - 0.6X_0$.

Figure 9.6 is a not-to-scale schematic of a single crystal, showing the layered crystal wrappings, silicon photodiodes, diode carrier plate, preamplifier and the aluminum housing enclosing the items at the crystal rear face. The existing photon detector consists of two $2 \times 1\,\mathrm{cm}^2$ silicon PIN diodes glued to a transparent 1.2 mm-thick polysterene substrate that, in turn, is glued to the center of the rear face of the crystal by an optical epoxy to maximize light transmission. The surrounding area of the crystal face is covered by a plastic plate coated with white reflective paint. The plate has two 3 mm-diameter penetrations for the fibers of the light pulser monitoring system.

The signal from each of the diodes is transmitted to the preamplifier through a cable terminated in a connector which allows straightforward decoupling of the preamplifier from the photodiodes. The entire assembly at the crystal's rear face is enclosed in an aluminum housing which is electrically coupled to the aluminum foil wrapped around the crystal, as well as thermally coupled to the support frame to dissipate the heat load from the preamplifiers.

The barrel crystals are inserted into modules that are supported individually from an external cylindrical support structure. At Babar, the barrel support cylinder carries the load of the barrel modules plus the forward endcap to the magnet iron through four flexible supports, which decouple and dampen any acceleration induced by movements of the magnet iron during a potential earthquake.

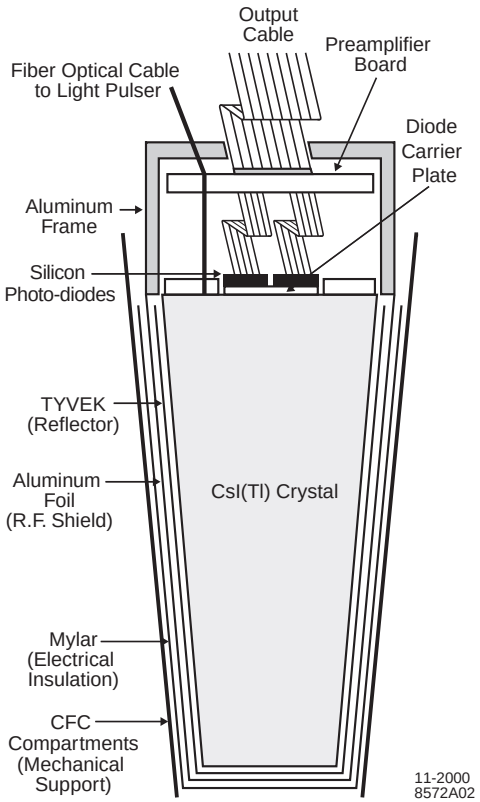

Figure 9.6: A schematic (not to scale) of a wrapped barrel crystal and the front-end readout package mounted on the rear face. Also indicated is the tapered, trapezoidal CFC compartment, which is open at the front.

The crystal modules are built from tapered, trapezoidal compartments made from carbon-fiber-epoxy composite (CFC) with 300 μm-thick walls. Each compartment loosely holds a single wrapped and instrumented crystal, assuring that the forces on the crystal surfaces never exceed its own weight. Each module is surrounded by an additional layer of 300 μm CFC to provide additional strength. The modules are bonded to an aluminum strong-back that is mounted on the external support structure. Figure 9.7 shows some details of a module and its mounting to the support cylinder. This scheme minimizes inter-crystal materials while exerting minimal force on the crystal surfaces, preventing geometric deformations and surface degradation that could compromise performance.

The barrel is divided into 280 separate modules, each holding 21 crystals (7×3 in $\theta \times \phi$), except for the furthest backward modules which are only 6×3. After insertion of the crystals, the aluminum readout frames, which also stiffen the module, were attached with thermally-conducting epoxy to each of the CFC compartments. The entire $\sim$ 100 kg module is then bolted and again thermally epoxied to an aluminum strong-back, which is shown in Figure 9.7. The strong-back contains alignment features as well as channels that couple to the cooling system. Each module was installed into the 2.5 cm-thick, 4 m-long aluminum support cylinder, and subsequently aligned. On each of the thick annular end-flanges, the support cylinder contains access ports for digitizing electronics crates with associated cooling channels, as well as mounting features and alignment dowels for the forward endcap. Figure 9.7 shows details of an electronics mini-crate situated within the support cylinder.

The primary heat sources internal to the calorimeter are the preamplifiers (2×50) mw/crystal and the digitizing electronics (3 kw per end-flange). In the barrel, the preamplifier heat is removed by conduction to the module strong backs which are directly cooled by Fluorinert (polychlorotrifluoro-ethylene). The digitizing electronics are housed in 80 mini-crates, each in contact with the end-flanges of the cylindrical support structure. These crates are indirectly cooled by chilled water pumped through channels milled into the end-flanges close to the inner and outer radii.

The entire barrel is surrounded by a double Faraday shield composed of two 1 mm-thick aluminum sheets so that the diodes and preamplifiers are further shielded from external noise. This cage also serves as the environmental barrier, allowing the slightly hygroscopic crystals to reside in a dry, temperature-controlled nitrogen atmosphere.

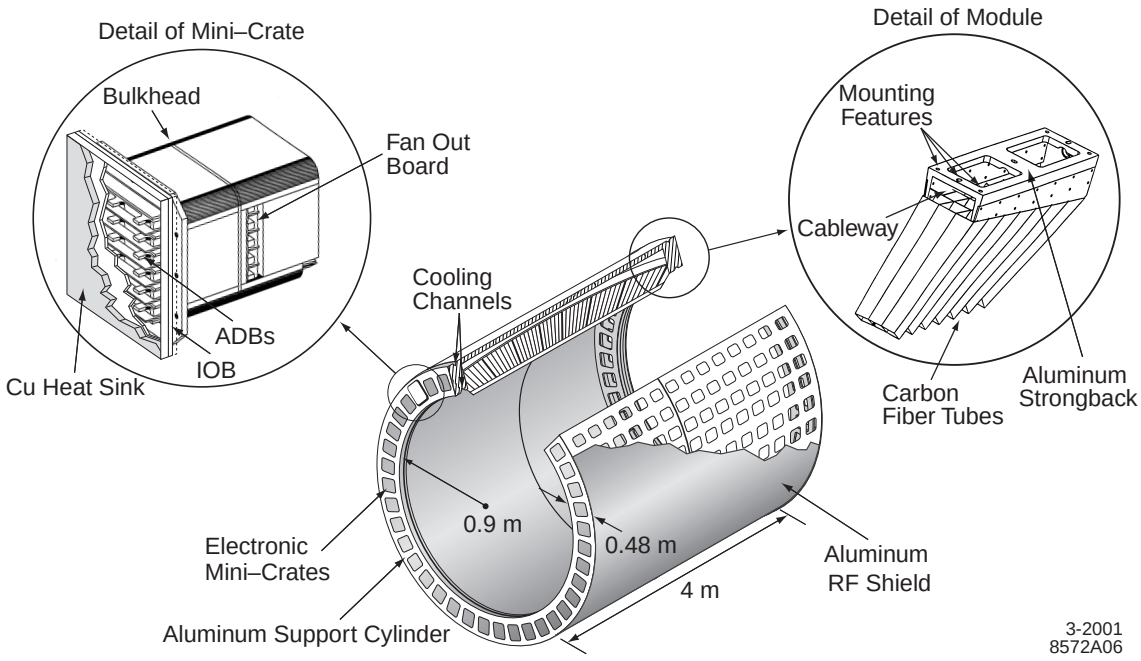

Figure 9.7: The EMC barrel support structure, with details on the modules and electronics crates (not to scale).

Similar to how it has been maintained throughout its existence, the EMC barrel is currently stored at a constant, accurately monitored temperature, During Babar data-taking, of particular concern were the stability of the photodiode leakage current, which rises exponentially with temperature, and crystal light yield, which is weakly temperature dependent. Currently, the most important issue is that the large number of diode-crystal epoxy joints experience as little stress as possible due to differential thermal expansion.

9.2.2.2 Readout

9.2.2.3 Calibration

9.2.3 Performance of BABAR barrel

As described in previous sections, SuperB EMC reuses the barrel part of of Babar EMC, consisting 5760 CsI (TI). Therefore, SuperB EMC performance is expected to be same as Babar, [**?**].

9.2.3.1 Energy and position resolution

The calorimeter is designed for excellent efficiency, energy and angular resolutions over the energy range 20MeV to 9 GeV. These requirements the choice for BABAR of a CsI(Tl) crystal calorimeter. The energy resolution of a homogeneous crystal calorimeter is given empirically as two terms summed in quadrature:

$$\frac{\sigma_E}{E} = \frac{a}{\sqrt[4]{E(GeV)}} \oplus b; \qquad (9.1)$$

where E and σ_E refer to the energy of a photon and its' RMS error in GeV. The energy dependent term, a, arises from fluctuations in photon statistics, electronics noise, and beambackground generated noise. The constant term, b, arises from non-uniformity in light collection,leakage or absorption in the material between and in front of the crystals, and uncertainties in thecalibration. The angular resolution is determined from the transverse crystal size and distance

Figure 9.8 shows the energy and angular resolution of the calorimeter derived from a variety of processes: radioactive source, symmetric 0

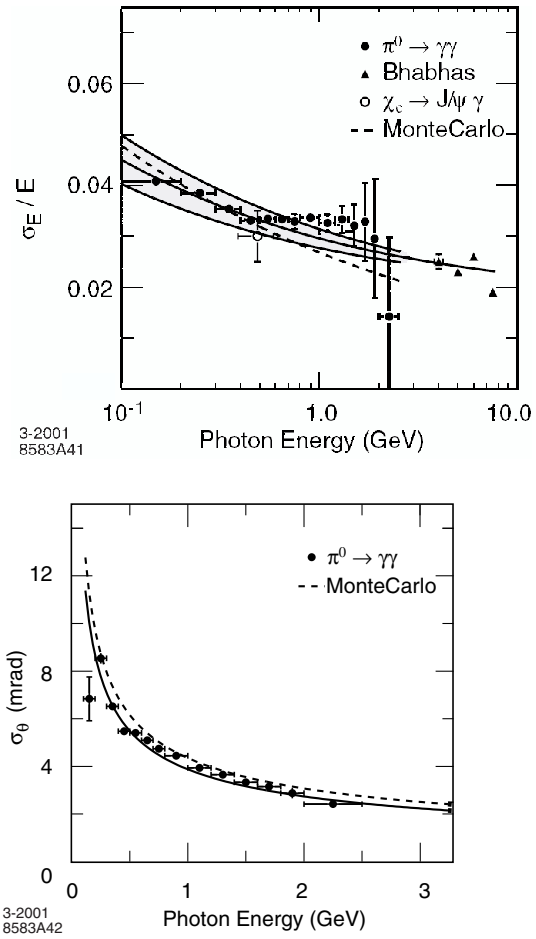

Figure 9.8: *photon energy (top) and angular (bottom) resolution from Babar experiment.*

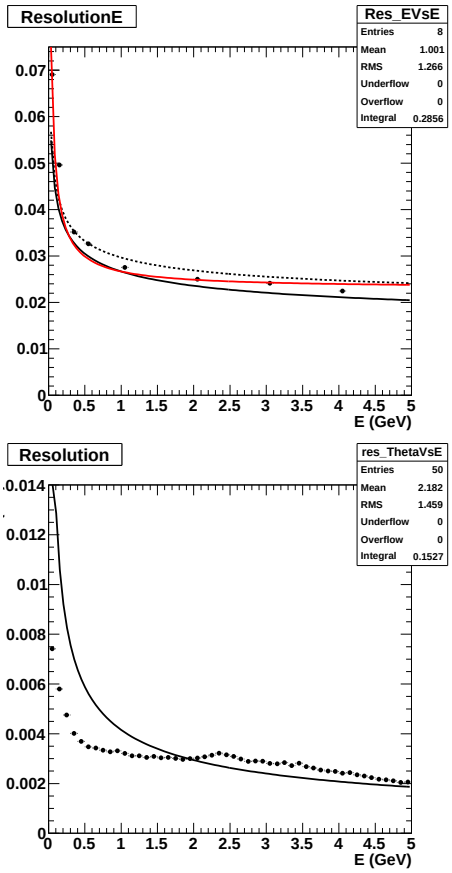

Figure 9.9: *photon energy (left) and angular (right) resolution from Babar experiment.*

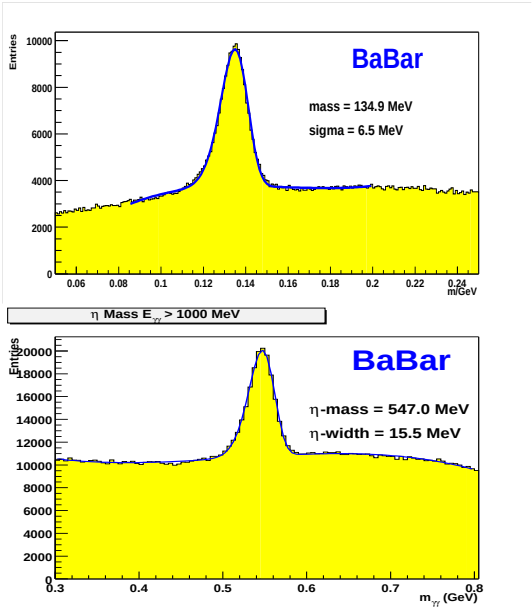

Figure 9.10: *Invariant mass spectrum of two photons for π^0 mass (top) and η mass (bottom).*

and decays, c1 ! J= , and Bhabha events.As the energy resolution of the 0 and is dependent on the calorimeter angular resolution,a simultaneous t to energy and angular resolution was done for those cases, assuming anasymmetry of the photon energy distribution derived from Monte Carlo. A smearing of the MC energies is applied in order to have good agreement between Data and MC. The data from the radioactive source calibration shows a deviation form the tted curve, as the photons from this process develop in single crystals and do not traverse material in front of the calorimeter. The angular resolution (Fig 4b) is derived from symmetric 0 and decays. Fits to the data yield

$$\frac{\sigma_E}{E} = \frac{(2.30 \pm 0.03 \pm 0.3)\%}{(E(GeV))^{0.25}} \oplus (1.35 \pm 0.08 \pm 0.2)\% \tag{9.2}$$

$$\sigma_\theta = \sigma_\phi = \frac{(4.16 \pm 0.04) mrad}{\sqrt{E(GeV)}} \oplus (0.0 \pm 0.0) mrad \tag{9.3}$$

Figure 9.9 is the similar plots from SuperB Fastsim. We can see a clear discrepance in the angular resolution due to im-perfect of Fastsim.

9.2.3.2 Gamma-gamma mass resolution

Figure 9.10 shows that two-photon invariant mass for hadronic events around the 0 mass in datafrom 2001. Photons are required to exceed 30MeV, while the 0 energy is required to exceed300MeV. The reconstructed mass is measure to be 134.9 MeV=c2, with a width of 6.5MeV=c2.The two-photon invariant mass for symmetric 's for E ¿ 1 GeV is shown in Fig 3b. Thereconstructed mass is 547MeV=c2, with a width if 15.5MeV=c2.

9.2.3.3 Radiation Damage Effects on Resolution

Radiation Monitoring Beam generated backgrounds are the major cause of reduction in the light yield of the crystal sover time. In order to monitor this source of background, 116 Rad FETs are placed in front of the calorimeter barrel and endcap crystals. These RadFETs are real-time integrating dosimeters based on solid-state MOS technology and are integrated into the EPICS monitoring system.As can be seen by Fig 6, the integrated dose is largest in the endcap which is closer the the beam line as well as more forward in polar angle making it more susceptible to beam generated background photons from small angle radiative Bhabha events in which an e strikes a machine element.F

The predominant radition damage effect in crystal scintillators is the radiation-induced absorptions, or color center formation, not the loss of scintialltion light yield.

Radiation damage impacts CsI(Tl) through the creation of color centers in the crystals, resulting in a degradation of response uniformity and light yield. The nominal dose budget for the *BABAR* CsI(Tl) calorimeter is 10krad over the lifetime of the detector. Pure CsI and L(Y)SO are considerably more radiation hard (see Table **??**). The dominant contribution to the dose arises from luminosity and single-beam background sources, and hence is due to MeV-level photons and (presumably) neutrons; the integrated dose scales approximately linearly with

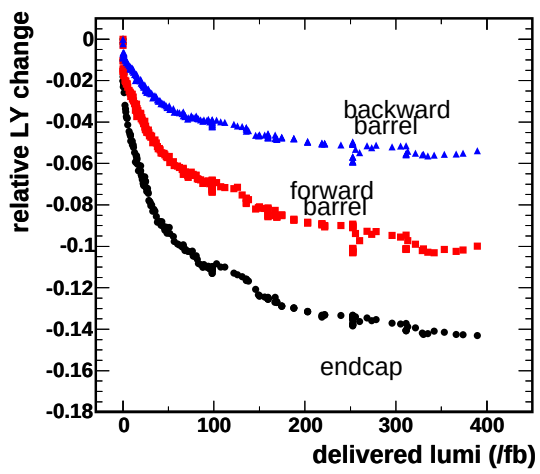

Figure 9.11: The light yield loss in the *BABAR* CsI(Tl) crystals due to radiation damage as a function of luminosity. The total dose received after 300 fb^{-1} is 1.2krad in the endcap and 750rad in the barrel.

integrated luminosity. The measured reduction of light yield due to radiation damage is shown as a function of integrated luminosity in Fig. 9.11. To date, a total dose of about 1.2krad has been received in the most heavily irradiated regions, resulting in a loss of about $\sim 15\%$ of the total light yield, but with no measurable impact on physics performance. It is notable that most of the observed light loss occurred relatively early in *BABAR* running, although radiation dose has been accummulating relatively steadily, and that crystals from different manufacturers have responded somewhat differently to irradiation. It is anticipated that the CsI(Tl) barrel will have accumulated approximately 1.5krad in the most irradiated regions by the end of nominal *BABAR* running in 2008. In order for the barrel calorimeter to function in the Super$B$ environment, beam background rates must be maintained at a level of approximately 1 MeV/μs or less per CsI(Tl) crystal. If this condition is achieved, then radiation dose rates are anticipated to be roughly comparable to current *BABAR* levels. A dose budget of well under 1 krad/year is expected to be achievable. At this a level, the CsI(Tl) barrel would survive for the duration of Super$B$ operations. This assumption will, however, need to be verified by detailed simulation.

9.2.3.4 Expected Changes in Performance at SuperB

The CsI(Tl) crystals used in the barrel calorimeters of both *BABAR* and Belle are the most expensive elements of the two detectors. Based on the performance that has been achieved, and the radiation damage that has been observed so far, both collaborations have concluded that the reuse of the barrel crystals is possible at a Super B Factory.

The baseline assumption is that the geometry of the crystals is unchanged from that of the current *BABAR* detector. The one change that should be made is to move the position of the interaction point from -5cm to +5cm relative to the position of the crystal gap normal to the beam axis. This adjustment retains the current non-pointing geometry, but moves the barrel to a slightly more symmetric position, in view of the reduced energy asymmetry. The effect of the change in boost from $\gamma\beta = 0.56$ to 0.28 and the shift of the IP is to increase the angular coverage of the barrel from 79.5% ($\cos\theta = -0.931$ to $+0.661$) to 84.1% ($\cos\theta = -0.883$ to $+0.798$).

If the crystal geometry is unchanged, it is possible to transport the entire barrel calorimeter as one cylinder. Alternatively it could be disassembled into its 280 individual modules, which would be transported separately and reassembled on arrival. It would only be necessary to disassemble the modules themselves if changes were being made to the material between the crystals, or to the photodiode readout. The costs of these alternatives are discussed in the chapter on the re-use of existing *BABAR* detector elements.

A possible change to improve the coverage in the backward region would be to add one or two additional rings of crystals to the last module ring in θ, which currently only contains 6 rings of crystals. However, this would lead to

major changes in the mechanical support structure and a redesign of the electronics readout, so it will not be undertaken unless there is a significant gain from the extra ring(s). Changes to the rear sectionof the barrel also clearly interact strongly with the possible addition of a backward endcap calorimeter (see below).

9.2.4 Electronics changes

The EMC barrel reuses the originals 5760 crystals from Babar. The crystals are coupled to a couple of PIN (Hamamatsu S2744-08) diodes glued to the large area of the crystal face. The possibility to change these photo-detectors with new devices was investigated, but the strong mechanical constraints and the impossibility to unglue the PIN photodiodes without the risk to damage something, obliged us to maintain the original photo-detectors. Each PIN diode in Babar is read with a separate electronic chain composed of a charge sensitive preamplifier and a CR-RC-RC shaper, with 800 ns -250 ns -250 ns shaping time. The output of each channel is amplified in two chains respectively with a gain of 1 and 32.

9.2.4.1 Rationale for changes

In the SuperB configuration we want to substitute all the Front End Boards of the Barrel Calorimeter. The new Front End Boards use off-the-shelf components in order to have a shorter integration time of the order of less than one microsecond. Mechanical constraints obliged to use the same form factor of the original Babar Front End Board. The necessity to reduce the integration time comes from a more intense background radiation in the SuperB environment. A shorter integration time means less photons from crystals but avoid also photons coming from off time events generated from background. For using a shorter integration time we need also to reduce the shaping time from the order of one microsecond to few hundreds of nanoseconds. Different tests and simulations were performed to understand better how to change the integration and shaping time. The need to have a good time signal to use in the EMC trigger focused the design of the charge preamplifier to a Transimpedence amplifier with a low feedback capacitance The choice to use a lower integration and shaping time decreases the background noise due to the background radiation but decreases also the number of photons collected from the scintillator, with a worse resolution due to less signal. Moreover a shorter shaping time increase the noise due to a larger bandwidth of the shaper.

The design of the preamplifier needs a special care to obtain a lower noise from the beginning by choosing low noise components. We expect also an increase of the power consumption of the new Front End Boards due to the use of larger bandwidth operational amplifiers and of off-the-shelf components.

9.2.4.2 Electronics design

The readout of each PIN diode is done using two separate channels. This choice is motivated from the necessity to have an high redundancy and minimize the possibility to have dead channels in case of a PIN diode break. In order to minimize the noise of the Front End Boards we provided two outputs for each channel, one for the low range energy and the other for high energy range, with a gain of 1 and 32 as in Babar. The idea to use only one gain in the Front-End was dropped, because using shorter integration times give smaller signals than Babar. Consequently we have to improve signal to noise ratios from the beginning, avoiding passing low level signals in long cables. The four signals for crystals (two channels with two different gain) are combined in the digitizer board; normally the mean signal from two PINs is chosen but in case of break of one PIN only one signal can be chosen. A dedicated circuit choice the signal range to use for the digitalization. The digitalization is done using a 12 bits ADC, with a shaping time of 500 ns, a sampling rate of 7.43MHz (RF /8) plus a range bit. If full granularity data were pushed synchronously to the trigger, about 520 optical links would be necessary. The number of synchronous trigger links can be drastically reduced by performing sums of 4 3 cells on the detector side, so that 6 such energy sums could be continuously transmitted

through a single optical serial link. This permits a reduction in the number of trigger links so as to match the topology of the calorimeter electronics boxes, which are split into 40 sectors on both sides of the detector. Therefore, the total number of links would be 80 both for the trigger and the data readout toward the ROMs, including a substantial safety margin (¿ 1:5).

9.2.5 SLAC De-installation, Transport and Local Storage

9.2.6 Electronics refurbishment

Repair crystals with 0/1 working channels

Preamp replacement

ADC board replacement

9.2.7 Calibration systems

Brief system description

Replace DT neutron generator

New plumbing from generator to detector

Repair and reconstitute light pulser system

9.2.8 Re-installation at Tor Vergata

Bibliography

[1] R. Y. Zhu, Nucl. Instrum. Meth. A **413**, 297 (1998).

9.3 Forward Calorimeter

The Forward Calorimeter is designed to extend the coverage of the electromagnetic calorimeter to low angles, as detailed in Tab. 9.1. To be effective its performances need therefore be comparable with the Barrel Calorimeter. Thus, the design considers a calorimeter made of homogeneous crystals and read-out by compact photodetectors capable of operating in magnetic field.

Taking as benchmark the BaBar detector, the relative energy resolution need be at most 4.3% at 100 MeV and 2.7% at 1 GeV. Also, in order to assure appropriate resolution on the π^0 invariant mass and to allow the $\pi^0 \to \gamma\gamma$ reconstruction up to sufficiently high energies, a segmentation at least comparable with the BaBar one is needed. Since the transverse crystal size is dictated by the Molier radius of the material, only crystals with a Molier radius at most as large as the CsI(Tl) can be considered. Finally hermeticity is also important, so the requirement on mechanics is that the fraction of particles originating from the interaction point passing through the cracks of the

As already described for the Barrel Calorimeter, the most stringent constraints come from the presence of large background due to the extremely high luminosity. As shown in Fig. 9.3, the expected dose integrated in a year ranges from $\sim$ 200 rad for the outermost rings to $\sim$ 2500 rad for the innermost ones. Consequently, the dose rate the crystals need to tolerate ranges from $\sim$ 0.1 rad/s to $\sim$ 1.0 rad/s, respectively.

As described in Sec. 9.1.1, the large rate of low energy photons can create radiation damage on the crystal themselves, thus reducing the light yield, and induce a degradation of the energy resolution due to pile-up. Therefore the chosen crystal must show a stable light yield under the expected radiation and the signal shape produced by the readout must be compatible with the expected rates.

In this section several combinations of crystals and electronics will be studied and the relevant properties will be studied. Eventually in Sec. 9.3.12.4 all the information will be folded together to verify the compliance with these requirements. The best option from the performances point of view is to use crystals made of LYSO readout by Avalance Photo-Diodes (APD) and this configuration has been studied in detail. Budget restrictions though forced us to consider as baseline for the cost estimates the solution closest to the full LYSO option but with a reasonable cost: the so-called "hybrid" option to keep the BaBar crystals, made of $CsI(Tl)$, in the outermost layers and replace the innermost layers, where the radiation issues are more severe, with LYSO crystals.

9.3.1 LYSO Crystals[RZ]

In the last two decades, cerium doped lutetium oxyorthosilicate (Lu_2SiO_5 or LSO) [1] and cerium doped lutetium yttrium oxyorthosilicate ($Lu_{2(1-x)}Y_{2x}SiO_5$ or LYSO) [2] have been developed for the medical industry with mass production capabilities established. This section addresses the issues of crystal properties, specifications, production and testing.

9.3.2 Introduction

Table 9.2 [3] lists basic properties of heavy crystals: NaI(Tl), CsI(Tl), pure CsI, bismuth gemanade ($Bi_4Ge_3O_{12}$ or BGO), lead tungstate ($PbWO_4$ or PWO) and LSO/LYSO. All have either been used in, or are actively being pursued for, high energy and nuclear physics experiments, which are also listed in the table. The experiment names in bold refer to future crystal calorimeters. NaI(Tl), CsI(Tl), BGO, LSO and LYSO crystals are also widely used in the medical industry. Mass production capabilities exist for all these crystals.

Table 9.2: Properties of Heavy Crystal with Mass Production Capability

Crystal	NaI(Tl)	CsI(Tl)	CsI	BGO	$PbWO_4$	LSO/LYSO(Ce)
Density (g/cm^3)	3.67	4.51	4.51	7.13	8.3	7.40
Melting Point (°CC)	651	621	621	1050	1123	2050
Radiation Length (cm)	2.59	1.86	1.86	1.12	0.89	1.14
Molière Radius (cm)	4.13	3.57	3.57	2.23	2.00	2.07
Interaction Length (cm)	42.9	39.3	39.3	22.7	20.7	20.9
Refractive Index[a]	1.85	1.79	1.95	2.15	2.20	1.82
Hygroscopicity	Yes	Slight	Slight	No	No	No
Luminescence[b] (nm)	410	560	420	480	425	420
(at Peak)			310		420	
Decay Time[b] (ns)	245	1220	30	300	30	40
			6		10	
Light Yield[b,c]	100	165	3.6	21	0.30	85
			1.1		0.077	
d(LY)/dT[b,d] (%/°CC)	-0.2	0.4	-1.4	-0.9	-2.5	-0.2

Experiment	Crystal	CLEO	kTeV	L3	CMS	**Mu2e**
	Ball	*BaBar*		BELLE	ALICE	**SuperB**
		BELLE			PrimEx	**HL-LHC?**
		BES III			**Panda**	

a At the wavelength of the emission maximum.
b Top line: slow component, bottom line: fast component.
c Relative light yield of samples of 1.5 X_0 and with the PMT quantum efficiency taken out.
d At room temperature.

Because of their high stopping power, high light yield, fast decay time, small temperature coefficient and excellent radiation hardness, LSO and LYSO crystals have attracted a broad interest in the high energy physics (HEP) community [4, 5, 6, 7], and are chosen for the baseline material for the SuperB forward calorimeter. LSO and LYSO crystals from following vendors were tested during the R&D phase of the project: CTI Molecular Imaging (CTI), Crystal Photonics, Inc. (CPI), Saint-Gobain (SG), Sichuan Institute of Piezoelectric and Acousto-optic Technology (SIPAT) and Shanghai Institute of Ceramics (SIC).

9.3.3 Optical and Scintillation Properties

9.3.3.1 Transmittance and Emission

LYSO crystals of 20 cm (18 X_0) long are routinely produced in industry. They have good transmittance spectra. The left plot of Figure 9.12 shows longitudinal (green) and transverse (red) transmittance spectra measured for a rectangular LYSO sample with a dimension of $2.5 \times 2.5 \times 20$ cm (18 X_0). Significant red shift is observed in the absorption edge of the longitudinal transmittance as compared to the transverse transmittance, which is caused by internal absorption. The black line at the top is a fit to the theoretical limit of transmittance calculated by using refraction index assuming multiple bounces between two end surfaces and no internal absorption [8]. It overlaps with the transverse transmittance spectrum at wavelengths longer than 420 nm, indicating excellent optical quality of the crystal. Also shown in this plot is the photo-luminescence spectrum (blue) [9]. The fact that a part of the emission spectrum is at the wavelengths shorter than the absorption edge indicates that this part of the scintillation light is absorbed internally in the crystal bulk, usually referred to as self-absorption effect. There is no such self-absorption effect in other scintillation crystals commonly used for HEP calorimeters, such as BGO, CsI(Tl) and PWO [3]. While this self-absorption has little consequence to 6 mm long pixels used in medical instruments, it would affect light response uniformity for 20 cm long crystals used to construct the SuperB calorimeter. This effect will be discussed in section 9.3.4.

During the R&D phase for crystal development poor longitudinal transmittance was observed in some samples [10]. The right plot of Figure 9.12 shows that four samples (SIPAT-7 to SIPAT-10) have poor longitudinal transmittance between 380 nm and 500 nm, showing an absorption band. A further investigation shows that this absorption band is located at the seed end and is caused by point defects [9]. The investigation was further pointed to a bad seed used in their growth, indicating that these point defects are structure related. With rigorous quality control, LYSO crystals grown later at SIPAT (SIPAT-11 to SIPAT-16) show no absorption band at the seed end, as shown in the right plot of Figure 9.12. An increase of light output at about 30% was found after this problem was resolved. It thus is important to include in crystal specifications a requirement to crystal's longitudinal transmittance.

The left plot of Figure 9.13 shows typical quantum efficiencies of a PMT with multi-alkali cathode (Photonis XP2254b) and an APD (Hamamatsu S8664) [11]. Also shown in the figure are the photo luminescence spectra of

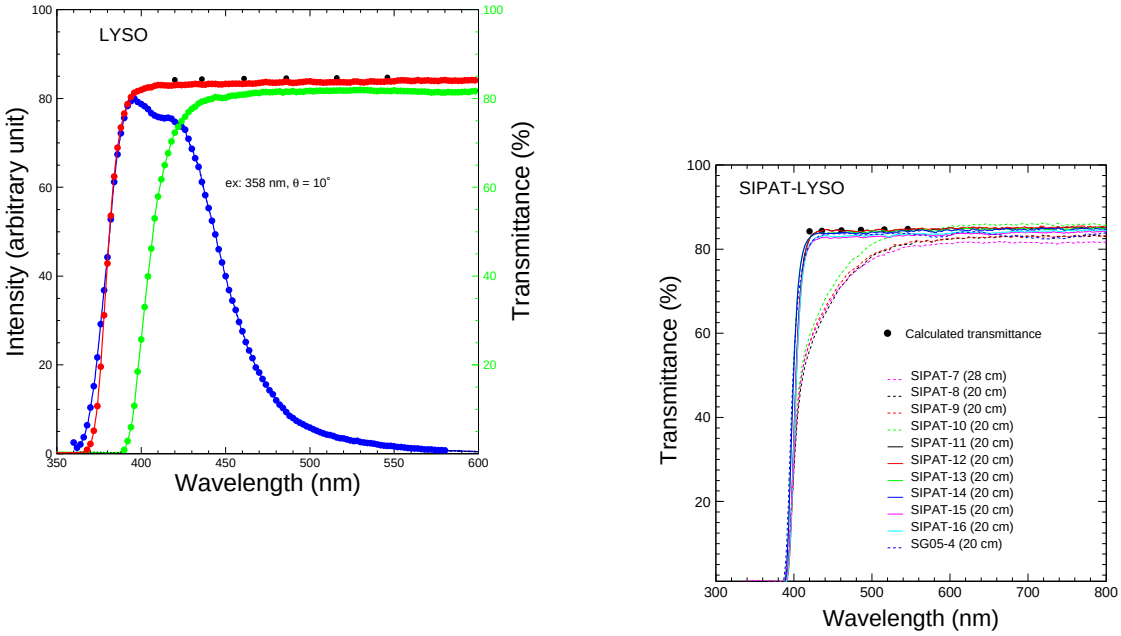

Figure 9.12: Left: The longitudinal (green) and transverse (red) transmittance spectra and the photo-luminescence (blue) spectrum are shown as a function of wavelength for a rectangular LYSO sample with a dimension of 2.5 × 2.5 × 20 cm. Right: Longitudinal transmittance spectra are shown as a function of wavelength for eleven LYSO crystals: ten from SIPAT and one from Saint-Gobain. All, except SIPAT-7, are 20 cm long.

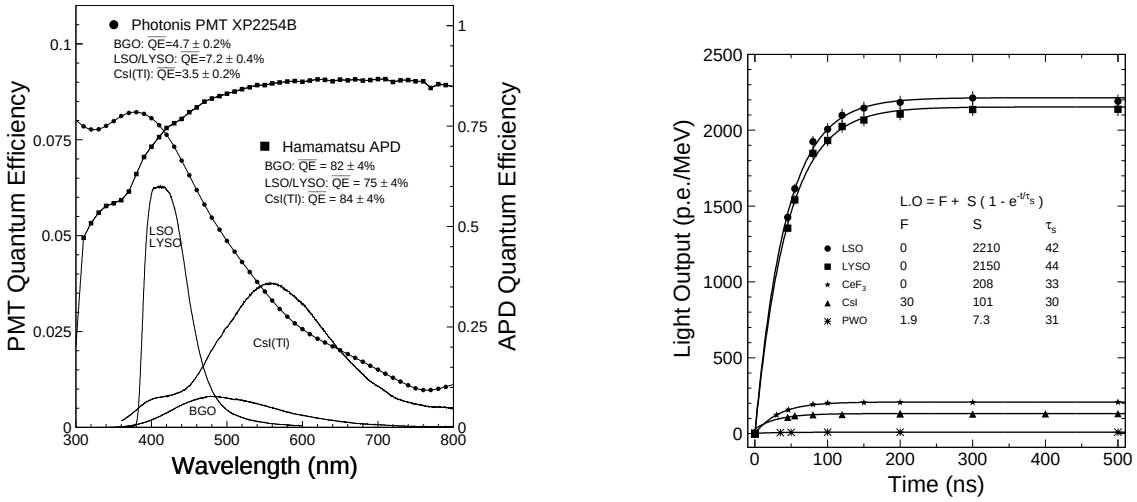

Figure 9.13: Left: The quantum efficiencies of a Hamamatsu R2059 PMT (solid dots) and a Hamamatsu S8664 APD (solid squares)are shown as a function of wavelength together with photo-luminescence spectra of the LSO/LYSO, BGO and CsI(Tl) samples, where the area under the luminescence spectra is roughly propotional to the corresponding absolute light output. Right: Light output measured by using a Photonis XP2254 PMT is shown as a function of integration time for six crystal scintillators.

LSO/LYSO, BGO and CsI(Tl) crystals, where the area under the luminescence spectra is roughly proportional to the corresponding absolute light output. Table 9.3 summarizes the numerical values of the photo luminescence weighted average quantum efficiencies for various readout devices. These numbers can be used to convert the measured photo-electron numbers to the absolute light output in photon numbers.

A significant red component was observed in the γ-ray induced luminescence spectra in the CTI LSO samples, but not in the LYSO samples from other growers [9]. This red component disappeared after a γ-ray irradiation with an accumulated dose of 5×10^3 rad. This is the only significant difference observed between the large size LSO and LYSO samples [9], indicating that LYSO is a preferred choice.

9.3.3.2 Decay time and Light Output

The right plot of Figures 9.13 shows light output in unit of photo-electron/MeV, measured by using a Photonis XP2254 PMT as a function of integration time, for six crystal scintillators [3]. The light output can be fit to the following function to determine the fast and slow components and the decay kinetics:

$$LO(t) = F + S(1 - e^{-t/\tau_s}), \qquad (9.4)$$

where F is the fast component of the scintillation light with a decay time of less than 10 ns, and S represents the slow component with a decay time of τ_s longer than 10 ns. It is clear that the decay time of both LSO and LYSO crystals is at a level of about 40 ns.

As shown in Table 9.2 LSO and LYSO crystals have high light output. It is about 85% and 50% of NAI(Tl) and CsI(Tl) respectively, and is about 18, 4 and more than 200 times of pure CsI, BGO and PWO, respectively. Figure 9.14 shows 0.511 γ-ray pulse height spectra measured by a Hamamatsu R1306 PMT (left) and two Hamamatsu S8664-55 APDs (right) for four LSO and LYSO samples of $2.5\times2.5\times20$ cm^3 from CTI, CPI, SG and SIPAT. The corresponding noise for the APD readout is less than 40 keV equivalent [11]. Poor energy resolution was found in the CPI LYSO sample, but not other samples. According to the grower this was caused by intrinsic non-uniformity which may be improved by appropriate thermal annealing. It thus is important to include in crystal specifications a requirement to crystal's energy resolution.

Because of their fast decay time and high light output, LSO and LYSO crystals have also been used in time of flight (TOF) measurements for medical applications, such as TOF PET(positron emission tomography). A better than 500 ps FWHM time resolution was achieved for the time difference between two photons. In HEP experiments a rms time resolution of better than 150 ps may be achieved for TOF measurements for single particles. Since the intrinsic rising time of scintillation light is about 30 ps for LSO and LYSO crystals [14], the measured time resolution for LSO and LYSO is affected mainly by the response speed of the readout device and the choice of time pick-off [13]. Doping calcium in LSO and LYSO is reported to reduce the decay time to about 20 ns [15], which would help to improve the time resolution.

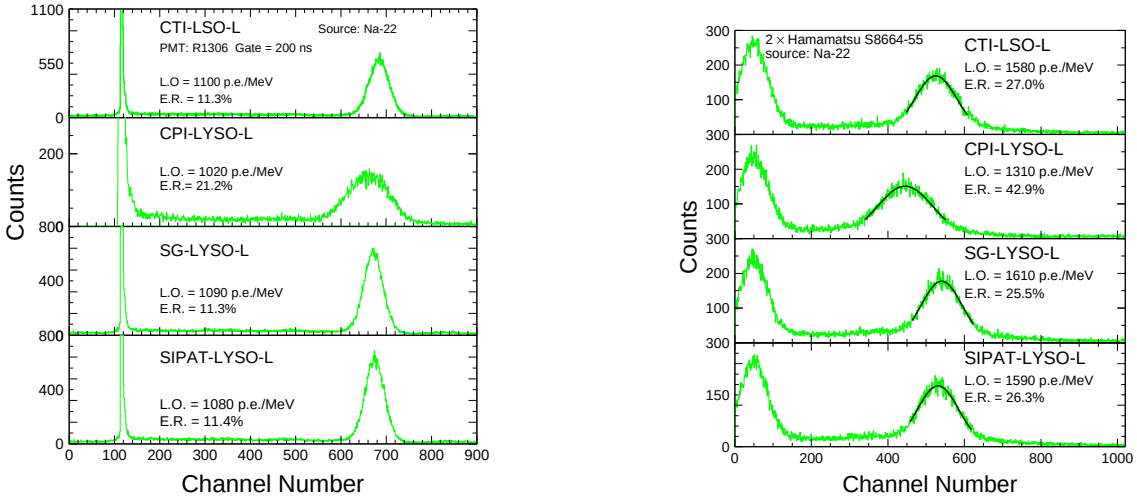

Figure 9.14: 0.511 MeV γ-ray spectra from a ^{22}Na source, measured by a Hamamatsu R1306 PMT (Left) and two Hamamatsu S8664-55 APDs (Right), with a coincidence trigger for four long LSO and LYSO samples of $2.5 \times 2.5 \times 20$ cm^3.

9.3.4 Light Collection and Response Uniformity

It is well known that adequate light response uniformity along the crystal length is key for maintaining the precision offered by a total absorption crystal calorimeter at high energies [16]. The light response uniformity of a long crystal as shown in Figure 9.15 (Left) is parameterized as a linear function

$$\frac{LY}{LY_{mid}} = 1 + \delta(x/x_{mid} - 1), \qquad (9.5)$$

where (LY_{mid}) represents the light output measured at the middle point of the crystal, δ represents the deviation from the flat response and x is the distance from the photo-detector. To achieve good energy resolution, the corresponding $|\delta|$ value for SuperB LYSO crystals of 18 X_0 must be kept to less than 3% [17].

Effective light collection requires good light reflector. The glass fiber based supporting structure designed for the superB forward calorimeter is coated with a thin layer of aluminum as reflector. All measurements and simulations discussed in this section are carrired out with aluminum coated glass fiber supporting structure cell, referred to as RIBA Cell, around the crystal.

The light response uniformity of a long tapered LSO/LYSO crystal is affected by three factors. First, the tapered crystal geometry leads to an optical focusing effect, i.e. the response for scintillation light originated at the

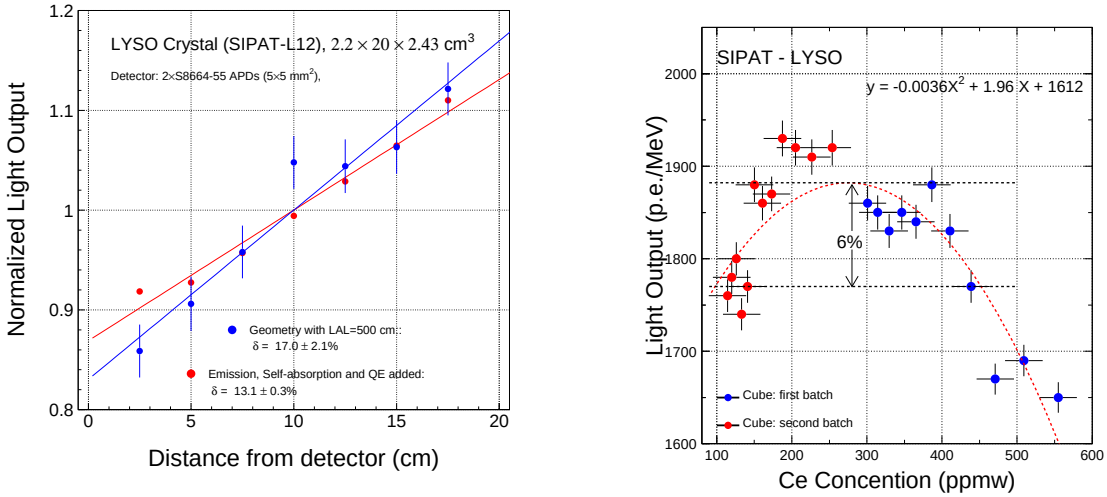

Figure 9.15: Left: Light response uniformities without (blue) and with (red) self-absorption effects, calculated by a ray-tracing program, are shown for a 20 cm long crystal with tapered geometry with two Hamamatsu S8664-55 APD readout. Right: Light outputs measured for 17 mm LSO/LYSO crystal cubes are shown as a function of the cerium concentration.

small end far away from the photo-detector would be higher as compared to that at the large end which is coupled to photo-detector. This is caused by the light propagation inside the crystal, and is common for all optical objects with such geometry. Second, there is a self-absorption effect in LSO/LYSO crystals as discussed in section 9.3.3.1 since a part of the emission spectrum is self-absorbed in the crystal bulk as shown clearly in the left plot of Figure 9.12. This effect is specific for LSO/LYSO crystals. Last, there is a non-uniform light yield along the longitudinal axis of the crystal. It is caused by the segregation process of the cerium activator in LSO/LYSO crystals during the growth. Because of the small segregation coefficient (about 0.2) the cerium concentration increases from the seed end to the tail end of the crystal. Such effect is common for all crystals doped with activator, e.g. CsI(Tl).

The left plot of Figure 9.15 shows the light response uniformities calculated using a ray-tracing program [16] for a SuperB LYSO crystal with tapered geometry and two Hamamat S8664-55 APD readout. While the blue dots show the uniformity with only the optical focusing effect the red dots show the same with the self-absorption effect also included. Numerically, the optical focusing effect alone causes a δ value of 17%, which is reduced to 13% with

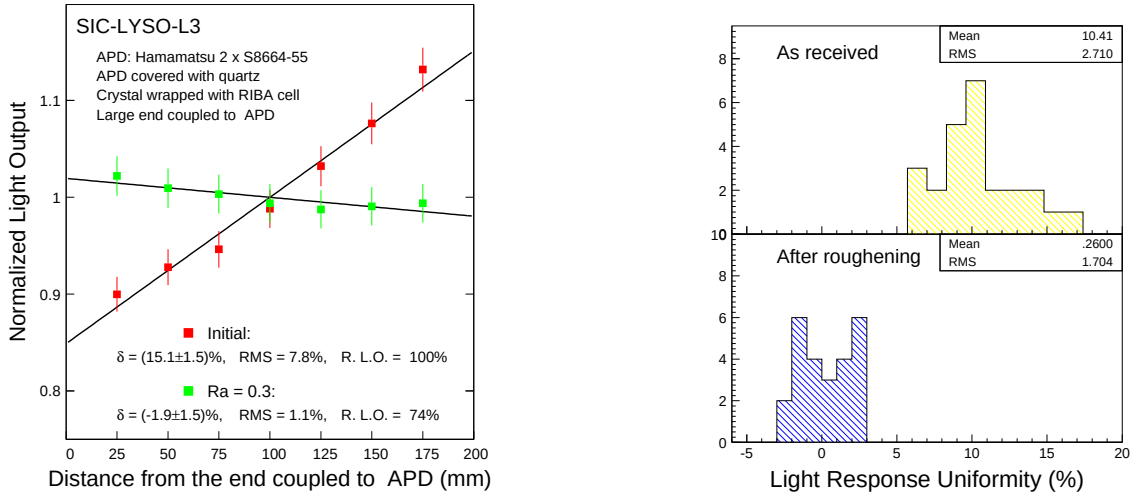

Figure 9.16: Left: Light response uniformity measured with two Hamamatsu S8664-55 APD readout for a tapered SuperB LYSO crystal SIC-L3 before (red dots) and after (green dots) uniformization by roughening the smallest side surface to Ra = 0.3. Right: The distributions of light response uniformity (δ values) are shown for 25 SuperB test beam crystals before (top) and after (bottom) uniformization by roughening the smallest side surface.

the self-absorption effect included. This indicates that the self-absorption effect provides a partial compensation for the optical focusing effect. The right plot of Figure 9.15 shows the light output measured for two batches of 17 mm LSO/LYSO crystal cubes (red and blue) as a function of the cerium concentrations determined by Glow Discharge Mass Spectroscopy (GDMS) analysis. It shows that the optimized cerium doping level is between 150 and 450 ppmw because of the interplay between the cerium activator density and the self absorption caused by the over-doping. Also shown in the plot is a second order polynomial fit. By adjusting the cerium doping the light yield difference along the crystal can be minimized. A difference at the level of 10% is more or less the maximum, which may provide a variation of the δ value up to 5%. Taking this into account the initial δ value of the SuperB LYSO crystals may vary between 8% to 18%.

Following the experiences of previous crystal calorimeters, such as L3 BGO and CMS PWO, a $|\delta|$ value of less than 3% may be achieved by roughening one side surface of the crystal to an appropriate roughness [18]. The left plot of Figure 9.16 shows the light response uniformities measured with two Hamamatsu S8664-55 APD readout for a tapered SuperB LYSO crystal SIC-L3. The δ value is reduced from 15% before (red) to -1.9% after (blue) roughening the smallest side surface to Ra = 0.3. The right plot of Figure 9.16 shows a comparison of the δ values before (top) and after (bottom) roughening for all 25 SuperB test beam crystals, showing a reduction of the average δ value from 10% to 0.26%. All 25 $|\delta|$ values after uniformization are within 3%. The reduction of light collection efficiency caused by this uniformization is about 17%. It is expected that one or maximum two Ra values would be sufficient to uniformize mass produced LYSO crystals to achieve $|\delta|$ values of less than 3%.

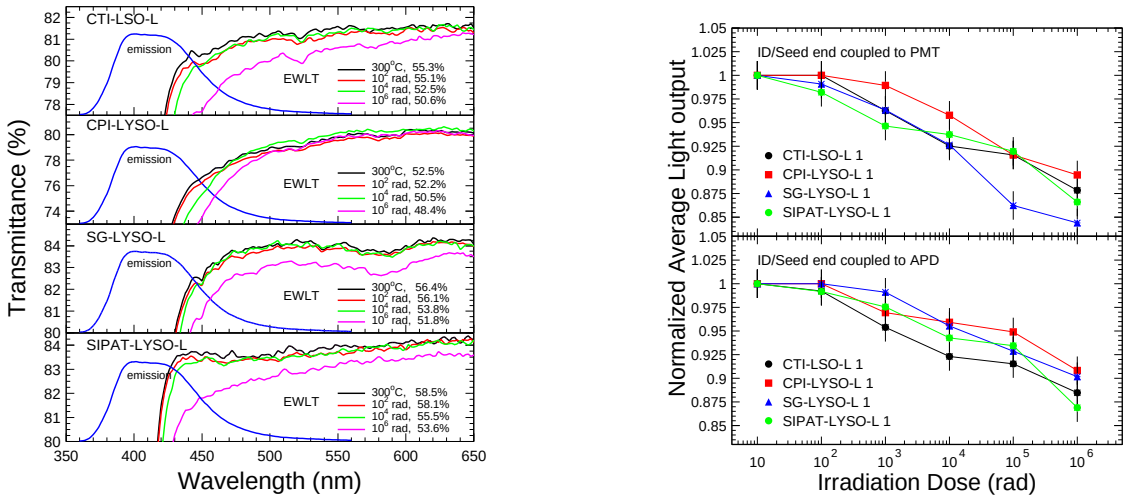

Figure 9.17: The longitudinal transmittance spectra in an expanded view (left) and the normalized light output (right) are shown as a function of the integrated dose up to 1 Mrad for four LSO and LYSO samples of $2.5 \times 2.5 \times 20$ cm^3. Also shown in the left plot is the photo-luminescence spectra (blue) in arbitrary unit.

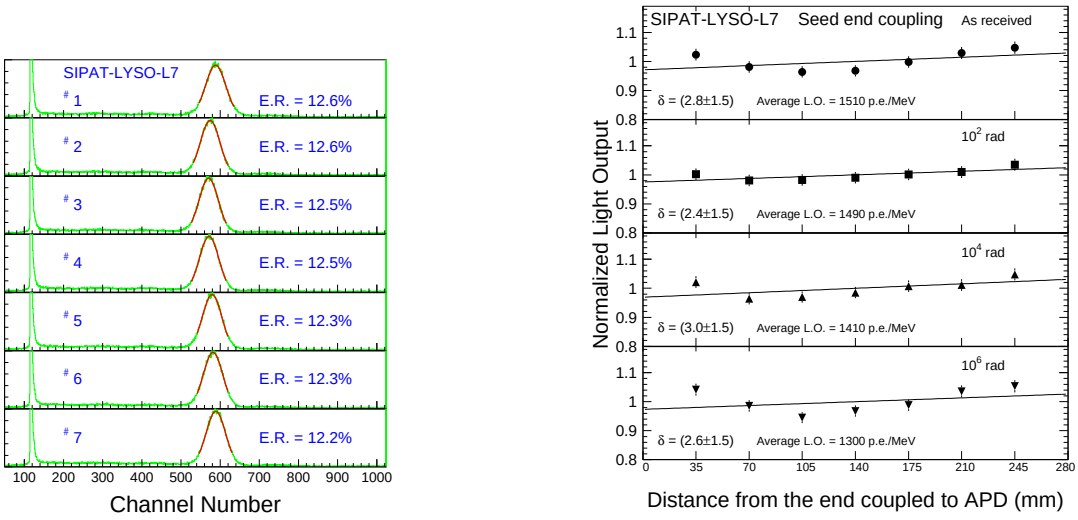

Figure 9.18: Left: The pulse height spectra of 0.511 MeV γ-ray peaks (green) and corresponding Gaussian fits (red) measured by a Hamamatsu R1306 PMT are shown at seven points evenly distributed along SIPAT-LYSO-L7. Also shown are the numerical values of the FWHM energy resolutions (E.R.). Right: Normalized light output and light response uniformity measured by two Hamamatsu S8664-1010 APDs, before and after γ-ray irradiations in several steps up to 1 Mrad are shown for SIPAT-LYSO-L7.

9.3.5 Radiation Hardness

The radiation hardness of long LSO and LYSO samples was investigated against γ-rays [19, 20] and neutrons [21]. It was found that the scintillation mechanism of this material is not damaged, its damage can be completely eliminated by thermally annealed at 300°C and does not recover at room temperature, indicating no dose rate dependence [16]. Studies also show that it is also more radiation hard against charged hadrons [22] than other crystals.

Figure 9.17 shows the longitudinal transmittance (left) and normalized average light output (right) for four 20 cm LSO and LYSO samples from CTI, CPI, SG and SIPAT. The light output was measured by using a XP2254 PMT (top) and two S8664-55 APDs (bottom). All samples tested have a consistent radiation resistance, with degradations of the emission-weighted longitudinal transmittance (EWLT) and the light output of approximately 12% for a γ-ray dose of 1 MRad. This radiation hardness is much better than other scintillation crystals, such as BGO, CsI(Tl) and PWO.

Recently, a 28 cm (25 X_0) LYSO crystal (SIPAT-LYSO-L7) was grown at SIPAT. This LYSO sample has consistent emission, adequate light response uniformity and good radiation hardness against γ-rays up to 1 Mrad [10]. The left plot of Figure 9.18 shows the pulse height spectra measured by a Hamamatsu R1306 PMT at seven points evenly distributed along SIPAT-LYSO-L7. The FWHM resolutions obtained for 0.511 MeV γ-rays from the ^{22}Na source are about 12.5%. This is quite good for crystals of such length. The right plot of Figure 9.18 shows normalized light output and response uniformity measured by two Hamamatsu S8664-55 APD before and after γ-ray irradiations with an integrated dose of 10^2, 10^4 and 10^6 rad. The degradation of the light output was found to be about 13% after 1 Mrad dose. The light response uniformity of SIPAT-LYSO-L7 does not change even after 1 Mrad dose, indicating that its energy resolution may be maintained [16].

In a brief summary, LSO and LYSO crystals are radiation hard crystal scintillator. Because of their excellent radiation hardness these crystals are expected to find applications in an environment where severe radiation environment is expected.

9.3.6 Specifications, Production and Testing

Following our extensive R&D on LYSO crystals, the following specifications are defined for the procurement of high quality LYSO crystals ffrom various vendors for the SuperB forward calorimeter.

- Dimension: +0.0/-0.1 mm.
- Longitudinal transmission at 420 nm: $>$ 75%.
- FWHM energy resolution: $<$ 12.5% for 0.511 MeV γ-rays measured by a Hamamatsu R1306 with DC-200 coupling at 7 points along the crystal.
- Light output will be required to be more than a defined percentage of a small crystal candle with air-gap coupling to PMT.
- Light Response uniformity ($|\delta|$): $<$ 3% measured by two Hamamatsu S8864-55 APDs.

Crystals will be produced by various vendors. The total crystal volume for the SuperB forward calorimeter is 0.36 m^3, which is small as compared to LYSO crystals grown for the medical industry. The following instruments are needed at each of the crystal vendors as well as the SuperB crystal laboratory.

- A station to measure crystal dimension.
- A photo-spectrometer with large sample compartment to measure the longitudinal transmission along 20 cm path.
- A PMT based pulse height spectrometer to measure light output and FWHM energy resolution with 0.511 MeV γ-rays from a ^{22}Na source.
- An APD based pulse height spectrometer to measure light response uniformity with 0.511 MeV γ-rays from a ^{22}Na source.

Table 9.3: Photo Luminescence Weighted Quantum Efficiencies (%)

Photo Luminescence	LSO/LYSO	BGO	CsI(Tl)
Hamamatsu R1306 PMT	12.9±0.6	8.0±0.4	5.0±0.3
Hamamatsu R2059 PMT	13.6±0.7	8.0±0.4	5.0±0.3
Photonis XP2254b	7.2±0.4	4.7±0.2	3.5±0.2
Hamamatsu S2744 PD	59±4	75±4	80±4
Hamamatsu S8664 APD	75±4	82±4	84±4

Bibliography

[1] C. Melcher and J. Schweitzer, "Cerium-doped lutetium oxyorthosilicate: a fast, efficient new scintillator," *IEEE Trans. Nucl. Sci.* **39** (1992) 502–505.

[2] D.W. Cooke, K.J. McClellan, B.L. Bennett, J.M. Roper, M.T. Whittaker and R.E. Muenchausen, "Crystal Growth and Optical Characterization of Cerium-doped $Lu_{1.8}Y_{0.2}SiO_5$," *J. Appl. Phys.* **88** (2000) 7360–7362, and T. Kimble, M Chou and B.H.T. Chai, "Scintillation Properties of LYSO Crystals," in *Proc. IEEE Nuclear Science Symposium Conference* (2002).

[3] R.H. Mao, L.Y. Zhang and R.-Y. Zhu, "Optical and Scintillation Properties of Inorganic Scintillators in High Energy Physics," *IEEE Trans. Nucl. Sci.* **NS-55** (2008) 2425–2431.

[4] W. Wisniewski, "Consideration for Calorimetry at a Super B Factory", in *Proceedings of Tenth International Conference on Calorimetry in Particle Physics*, Ed. R.-Y. Zhu, World Scientific (2002), and C. Cecchi. "A LYSO Calorimeter for a SuperB Factory ," in *Proceedings of Fourteenth International Conference on Calorimetry in Particle Physics*, Journal of Physics Series (2010).

[5] F. Happacher, "CCALT: Crystal Calorimeter at KLOE2," in *Proceedings of Fourteenth International Conference on Calorimetry in Particle Physics*, Journal of Physics Series (2010).

[6] The Mu2e Experiment, see http://mu2e.fnal.gov/.

[7] R.-Y. Zhu, Talk given at the CMS Forward Calorimetry Task Force Meeting at CERN, June 17, 2010. See http://indico.cern.ch/getFile.py/access?sessionId=0&resId=4&materialId=0&confId=97272

[8] D.A. Ma and R.-Y. Zhu, "Light Attenuation Length of Barium Fluoride Crystals," *Nucl. Instr. and Meth.* **A333** 422-424 (1993).

[9] R.H. Mao, L.Y. Zhang and R.Y. Zhu., "Emission Spectra of LSO and LYSO crystals Excited by UV Light, X-ray and γ-ray," *IEEE Trans. Nucl. Sci.* **55** (2008) 1759–1766.

[10] Rihua Mao, Liyuan Zhang and Ren-yuan Zhu, "Quality of a 28 cm long LYSO Crystal and Progress on Optical and Scintillation Properties," Paper N38-2 in *2010 IEEE NUCLEAR SCIENCE SYMPOSIUM CONFERENCE RECORD.*

[11] J.M. Chen, L.Y. Zhang and R.-Y. Zhu, "Large Size LSO and LYSO Crystal Scintillators for Future High Energy Physics Experiments," *IEEE Trans. Nucl. Sci.* **NS-54** (2007) 718–724 and *Nucl. Instr. and Meth.* **A572** (2007) 218–224.

[12] J.M. Chen, L.Y. Zhang and R.-Y. Zhu, "Large Size LYSO Crystals for Future High Energy Physics Experiments," *IEEE Trans. Nucl. Sci.* **NS-52** (2005) 3133–3140.

[13] R.-Y. Zhu, Invited talk given at the Time Resolution Workshop at University of Chicago, April 28, 2011. See http://www.hep.caltech.edu/∼zhu/talks/ryz_110428_t

[14] S.E. Derenzo, M.J. Weber, W. W. Moses, and C. DuJardin, "Measurements of the Intrinsic Rise Times of Common Inorganic Scintillators," *IEEE Trans. Nucl. Sci.* **47** (2000) 860–864.

[15] T. Szczesniak, M. Moszynski, A. Synfeld-Kazuch, L. Swiderski, M.A.S. Koschan and C.L. Melcher, "Time resolution and decay time of LSO Crystals Co-Doped with Calcium," *IEEE Trans. Nucl. Sci.* **57** (2010) 1329–1334.

[16] Ren-yuan Zhu, "Radiation Damage in Scintillating Crystals," *Nucl. Instr. and Meth.* **A413** (1998) 297–311.

[17] *The CMS Electromagnetic Calorimeter Project*, CERN/LHCC 97-33 (1997).

[18] Rihua Mao, Liyuan Zhang and Ren-yuan Zhu, "Optimization of Light Response Uniformity for SuperB Tapered LYSO Crystals with APD Readout," Paper N2 *2011 IEEE NUCLEAR SCIENCE S POSIUM CONFERENCE RECORD*.

[19] J.M. Chen, R.H. Mao, L.Y. Zhang R.Y. Zhu, "Gamma-ray induced radi damage in large size LSO and LYSO tal samples," *IEEE Trans. Nucl. Sci* (2007) 1319–1326.

[20] Rihua Mao, Liyuan Zhang and yuan Zhu, "Gamma-ray induced radi damage in PWO and LSO/LYSO tals," *2009 IEEE NUCLEAR SCIE SYMPOSIUM CONFERENCE REC* VOLS 1-5 (2009) 2045-2049.

[21] Rihua Mao, Liyuan Zhang and Ren- Zhu, "Effects of neutron irradiations i ious crystal samples of large size fo ture crystal calorimeter," *2009 IEEE CLEAR SCIENCE SYMPOSIUM FERENCE RECORD*, VOLS 1-5 (2041-2044.

[22] F. Nessi-Tedaldi, G. Dissertori, Lecomte, D. Luckey and F. P "Studies of Cerium Fluoride, LYSO and Lead Tungstate Crystals Exposed to High Hadron Fluences," Paper N32-3, 2009 IEEE NSS Conference.

9.3.7 Readout and Electronics[VB]

9.3.7.1 APD Readout[DH]

The photosensors chosen for readout of the LYSO crystals of the forward endcap are an independent pair of 10×10 mm avalanche photodiodes (APDs). The APDs have several advantages over photodiodes in this application: they are a better match to the emission spectrum of LYSO, providing a quantum efficiency integrated over the spectrum of 75% (see Figure 9.19); they provide useful gain (of the order of 75) with low noise; and, as they have a thinner sensitive region, they suffer less from the nuclear counter effect.

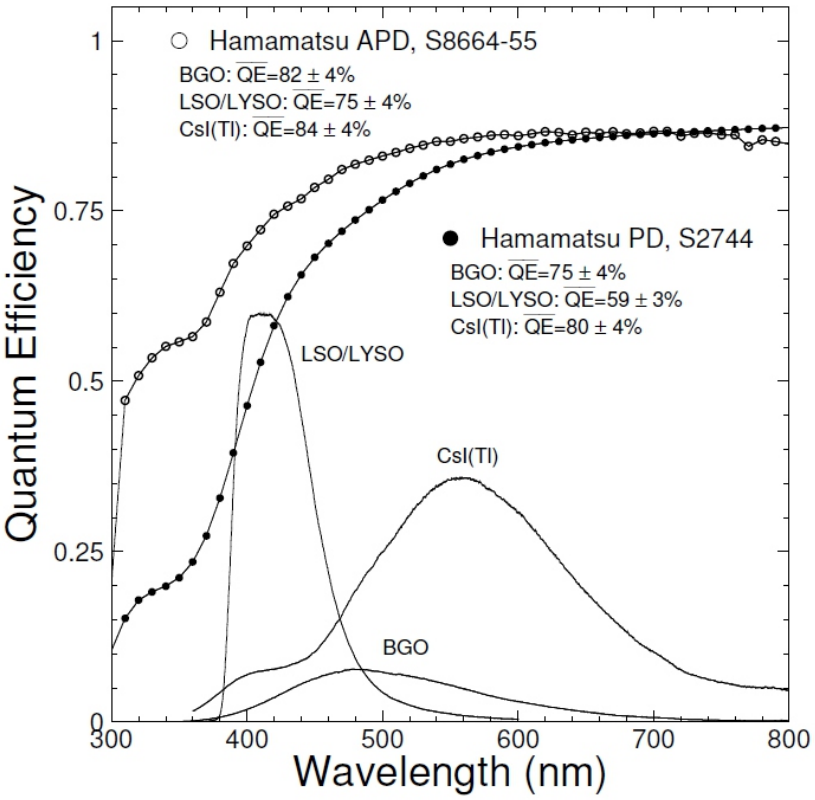

Figure 9.19: Quantum efficiency of a Hamamatsu APD and photodiode, together with the emission spectra of LYSO, BGO and CsI(Tl) crystals.

The gain with low noise of the APDs presents two additional advantages: it can allow a reduction of the shaping and integration time constants, constants that, as shown in Sec. **??**, can be used as a handle to fight the machine background; it improves the signal-to-noise ratio for the signals used for calibration (see Sec. **??**), allowing a crystal by crystal calibration (see Sec. 9.3.8).

9.3.7.2 Electronics Block diagram

9.3.7.3 Preamplifier

9.3.7.4 Shaper

9.3.7.5 Digitization

9.3.7.6 Requirements on mechanics

Cables, encumbrances, required cooling, ...

9.3.8 Calibrations[DH]

9.3.8.1 Initial calibration with source

A goal of the design is that the signal rate and the signal-to-noise ratio with a typical radioactive source such as ^{137}Cs be sufficient to allow individual calibration of each crystal with the readout device with which it will actually be paired. Photodiode readout of large crystals does not allow the use of sources for calibration and setup; this is typically done with a reference photomultiplier, with the results then convoluted with the results of individually calibrated photosensors. Such a procedure does not,of course, fully account for the effects of surface oxidation of the crystal or glue joint losses. With APD readout, the response of the entire chain can be measured.

The full setup of each crystal assembly requires each crystal/readout package to be individually adjusted to meet the uniformity requirements *in situ* and the characteristics of each object to be entered into a reference database. This involves appropriate roughening of, typically, one crystal surface to conform to a light collection uniformity specification ($\sim \pm 5\%$ over the forward 90% of each crystal) formulated to meet the energy resolution specification. The output of this setup/calibration procedure is then entered into a reference database, which serves as the initial set of calibration constants for the calorimeter system.

The fully assembled calorimeter is then calibrated with the circulated fluorinert system already used in BaBar (see Sec. 9.2.7) at appropriate intervals (one to four weeks in the case of *BABAR*). A substantial advantage of this approach is that there is an individual pedestal and gain constant for each crystal. A limitation is that the source is at a relatively low energy, although it is at a higher energy than that obtained from long-lived radioactive sources. This can be a problem in particular if using crystals with intrinsic radioactivity, such as for instance the LYSO. For such a crystal the calibration system needs to be properly designed to achieve the required accuracy in a sustainable time.

Calibration with radiative Bhabhas can overcome this limitation, but it requires development of a complex matrix unfolding procedure, since high energy electrons deposit shower energy in many crystals, not in a single crystal as in the case of source calibration.

9.3.8.2 Electronics calibration

9.3.8.3 Temperature monitoring and correction

The characteristics of APDs place fairly stringent requirements on the temperature control of the system, greater than those imposed by the temperature variation of light output of the crystals, as well as on the stability of the APD power supply voltage.

The Hamamatsu S-8664 APDs specified for the crystal readout have a temperature coefficient of gain of $\Delta G/\Delta T$ of 2.5%/°C, while the LYSO light output varies $-0.2\%/°C$. A specification of an APD gain stability of $\pm 0.5\%$ requires knowledge of the temperature to $\pm 0.2°C$. The CERN beam test demonstrated that a measurement of the calorimeter temperature to 0.2°C can be easily achieved. Furthermore the energy degradation due to machine background might allow to tolerate even a less stringent control.

As far as the overall structure is concerned we can keep the characteristics of the BaBar one. The entire calorimeter is surrounded by a double Faraday shield composed of two 1mm-thick aluminum walls, so that the diodes and preamplifiers are shielded from external noise. Such shield also served as an environmental enclosure, surrounding the slightly hygroscopic CsI(Tl) crystals with a dry, temperature controlled nitrogen atmosphere. The preamplifiers (2 50mW/crystal) and the digitizing electronics ($\sim$3 kW per end-flange) were the primary internal heat sources. The temperature was monitored by 256 thermal sensors distributed over the calorimeter. This system maintained the crystal environment at $20 \pm 0.5°C$. Dry nitrogen circulation stabilizes the relative humidity at $1 \pm 0.5\%$. This system can be extended to a forward endcap in a straightforward manner.

As far as gain stability is concerned, a gain of $\sim$75, with a reverse bias voltage of $\sim$375V, a voltage stability of better than 1 volt is required. This requirement can be met by commercially available computer-controlled high voltage supplies, such as those used for the CMS calorimeter.

9.3.9 Mechanical Structure[TZ/FP/VP]

This section will describe the issues related to reusing the mechanical structure of BaBar to support the hybrid solution for the FWD calorimeter.

9.3.10 Performance in simulations[Ch-Ch]

includes fastsim studies to optimize the number of CsI layers

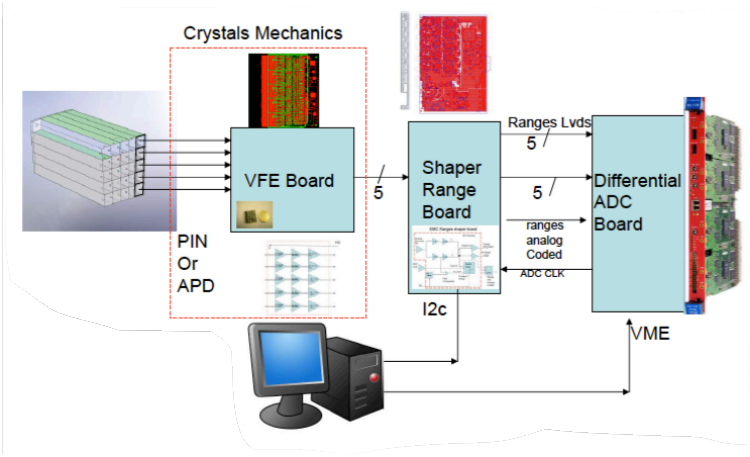

Figure 9.21: Schematic view of the electronic chain for the forward EMC.

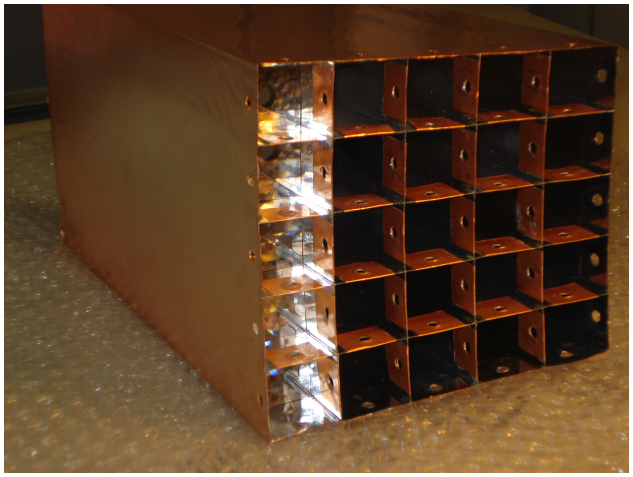

Figure 9.20: Picture of the Test Beam mechanical structure with one raw of LYSO crystals.

9.3.11 Tests on Beam[CC]

9.3.11.1 Description of apparatus

Two tests beam have been performed with a prototype LYSO matrix, one at CERN in October 2010 and one at the Beam Test Facility (BTF) in Frascati in May 2011. The prototype matrix is composed by 25 LYSO crystals of pyramidal shape with dimensions 2.3cm×2.3cm×22cm inserted in a support structure assembled by the RIBA company (Faenza, Italy) described in detail in Sec. 9.3.9. To improve light output uniformity, each crystal presents a black band of 15mm at the end of its smallest face and the area of the face not covered by the APD (or PiN) is painted with a reflective white painting. The mechanics is composed of glass fiber, covered with copper foils $35\mu m$ thick. Between one cell and the other there is a nominal thickness of 200 μm, while the external side has a thickness of 135 μm. Fig.9.3.11.1 shows a picture of the Test Beam structure with inserted one raw of crystals. Of the crystals, 20 are read out with an Avalanche Photodiode (APD) in both Test Beams while the remaining 5 are read out with PiN Diodes at the CERN Test Beam and with APDs at the BTF. As shown in Fig. 9.21, the readout chain is composed of: a front end board (VFE) that contains a Charge Shaper Preamplifier (CSP); Shaper Range Board which completes the attenuation, already applied in the VFE board, and then divides them according to the different energy range. Two different ranges are foreseen in

Figure 9.22: Schematic view of the test beam setup used at CERN.

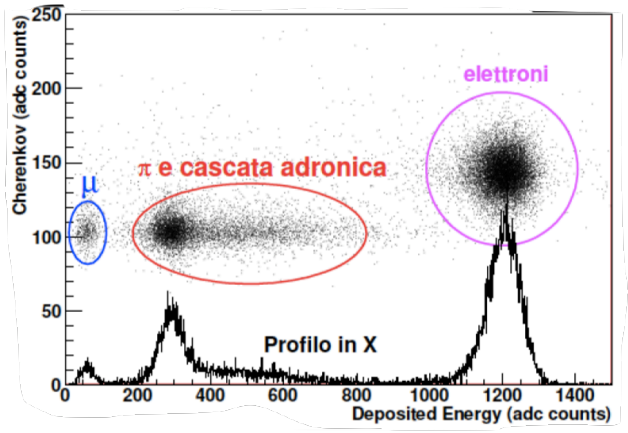

Figure 9.23: Distribution of the signal measured in the Cherenkov detector as function of the total energy deposited in the calorimeter, at 1 GeV.

the treatment of the signals, for energies lower than 200 MeV and for energies greater than 200 MeV, although in the test beams the amplifications have been adjusted to use only one range; a 12 bits Caen ADC to process the signals and digitize the analogue outputs. Two different configurations have been used at CERN for the power supply of the APD's, one called High Gain with voltage APD at 380V and one called Low Gain with a voltage of 308V applied.

MISSING TRIGGER

9.3.11.2 Description of the beams

The Beam Test at CERN has been performed at the T10 beam line in the East Area. The beam is mainly composed of electrons, muons and pions created by the scattering of protons into aluminum and tungsten target. The composition of the beam is highly dependent on the energy and for electrons it ranges from 60% at 1 GeV to 1% at 6 GeV. The maximum energy reachable at this beam line is 7 GeV with a nominal momentum spread $\Delta p/p \simeq 1\%$. The distance between the end of the beam line and the matrix is about 15 m. The event rate is of the order of 1 Hz.
Fig.9.22 shows the experimental setup used at CERN, it is composed of a Cherenkov detector already present in the CERN beam line, two scintillators (finger counters) $2\times2\text{cm}^2$, the box containing the matrix and the VFE boards. The Cherenkov detector plus the two scintillators of the fingers act as trigger. The Cherenkov detector allows the separation between electrons and pions as shown in Fig.9.23 . The same detector has also been used to select Minimum Ionising Particles (MIP) used for the calibration.
The Beam Test Facility in Frascati is part of the ΦFactory, DaΦne. It is composed of a linear accelerator LINAC, one spectrometer and two circular accelerators of electrons and positrons at 510 MeV. The LINAC is the same which supplies the test beam line at the BTF. The pulsed beam of the LINAC circulate electrons up to 800 MeV at a maximum current of 550 mA/pulsation and positrons at a maximum energy of 550 MeV with a current of 100 mA/pulsation. The typical duration of a pulsation is 10 ns, with a frequency of 50 Hz. A bending magnet select electrons of a given momentum, a line of about 12m contains quadrupoles for the uniformation of the beam and a system

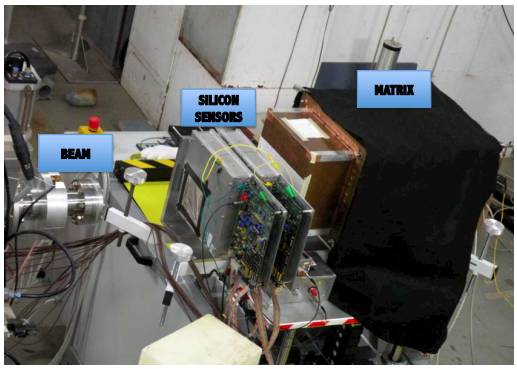

Figure 9.24: Schematic view of the test beam setup used at the BTF in Frascati.

of slits allow to change the flux of arriving particles. The beam energy spread is 1% at 500 MeV. The setup for the beam test of the matrix at the BTF is shown in Fig.9.24. The setup shows the end of the electron beam line, four planes of silicon strip detector (two measurements in x and two measurements in y) and the box containing the matrix with the crystals and the VFE boards. As mentioned before, at the BTF all the crystals are equipped with APD's, and it should be mentioned that the gain of the VFE has changed with respect to CERN from 0.5 to 1, while an amplification factor has been introduced. To control the position of the beam with respect to the matrix a detector of 16 x 16 scintillating fibers of 3mm each has been used. The trigger is performed by the LINAC radiofrequency (25 Hz), and does not make any use of scintillators.

Since the beam energy spread of the CERN facility proved to be significantly larger than the specifications, based on the performances of the detector at the BTF, we will use the CERN TB data only to study the linearity at high energy, while resolution studies will be performed exclusively on the BTF data.

9.3.11.3 Description of data and calibration

For each triggered event, the output of the readout are the waveforms of the 25 channels, each constituted by 384 samples. The signal amplitude in each channel is defined as the maximum of the waveform, extracted from a guassian fit to the sampling distribution, subtracted of a pedestal. For each crystal, the pedestal is calculated averaging the first 60 samples on a reference run. The pedestal-subtracted amplitude is considered to be the measurement of an energy deposit if it is above a threshold chosen to be three times the noise fluctuation, whose value is determined from a run taken with random triggers where no signal is present.

After calibration, the energy released in the whole matrix, the so-called cluster energy, estimate of the energy of the electron that initiated the shower, was estimated by summing all the energy deposits in all crystals.

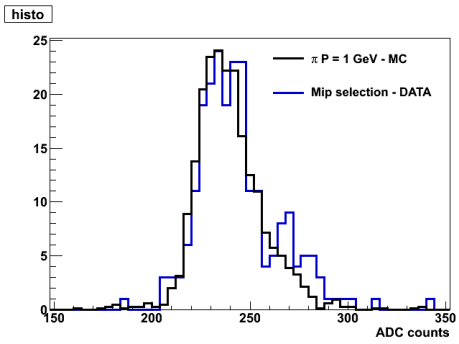

Figure 9.25: Comparison between data and MC of the energy deposited in the MIPs sample. The hypothesis that after the selection the beam is dominated by pions is made.

At the CERN test beam hadrons traversing the crystals horizontally were selected as Minimum Ionizing Particles (MIPs) by requiring no significant signal in the other crystals and a signal consistent with an hadron in the Cherenkov detector. Profiting from the fact that MIPs release a constant amount of energy regardless of their energy, the amplitude spectra of each crystal was fitted to extract the most likely value. After determining on the simulation the expected released energy in each crystal (Fig 9.26) , the corresponding calibration constants could be extracted.

At the BTF test beam, where no hadrons were available, the relative intercalibration constants were obtained on the electron sample itself. The relative cluster energy resolution was minimized by floating a constant in front of each crystal a part from the central one. The overall energy scale was then determined from the knowledge of the beam energy. This procedure was applied on a small fraction of the runs where the electrons were approximately 500 MeV (the highest energy reached in the tests) and the corresponding constants used in all other runs. This intercalibration was also cross-checked by means of cosmic-ray data obtained with an ad-hoc trigger made of two plastic scintillator pads positioned above and below the crystal matrix(see Fig. **??**). The channels where there is a significant difference are those where the electron data see very little energy because they are far from the center of the matrix. In such cases, that have little impact on the resolution studies since they contribute little to the total energy measurement, the MIPs intercalibrations are used.

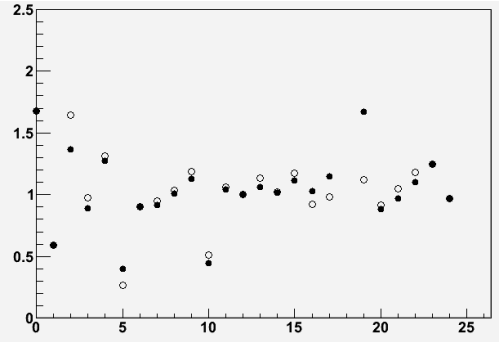

Figure 9.26: Comparison between electron and MIPs calibration at the BTF test beam as a function of the crystal number. Calibration constants are referred to crystal 12 that is therefore by definition equal to unity.

9.3.11.4 Electronics noise measurements

The first information we could extract from the data are the characteristics of the electronic noise. From the signal distribution in a random trigger run at the BTF we estimated (Fig. 9.27) that a part from two channels, the noise is on average 2ADC counts. After applying the calibration, this noise corresponds to approximately 0.4MeV. To understand if there were resonant components, the noise of each crystal i was analyzed in the Fourier space, by estimating its power spectrum from waveforms acquired with a random trigger:

$$\mathrm{PS}_i(\omega_k) =< n_i(\omega_k) n_i^*(\omega_k) > . \qquad (9.6)$$

The estimated power spectrum of a representative channel is shown in Fig. 9.27, where it can be seen that the dominant source of noise is in the range 0-8 MHz, which corresponds to the frequency bandwidth of the shaper. Sources of noise occurring after the shaper give a negligible contribution, while those occurring before are filtered according to the shaper transfer function and dominate.

We investigated the presence of a possible correlation between the noise observed on different crystals. The correlation can be in principle present, because the APDs in the matrix are biased by a unique power supply, and each Front End board serves 5 crystals.

The covariance between crystals i and j has been estimated as

$$\mathrm{COV}_{ij}(\omega_k) =< n_i(\omega_k) n_j^*(\omega_k) > \qquad (9.7)$$

The magnitude of an element of these matrices is the covariance between two crystals as usually intended in the real domain, while the phase is the relative time delay between them. As a consequence the correlation is also a complex quantity, which is defined as:

$$\rho_{ij}(\omega_k) = \frac{\mathrm{COV}_{ij}(\omega_k)}{\sqrt{\mathrm{PS}_i(\omega_k)\mathrm{PS}_j(\omega_k)}} . \qquad (9.8)$$

This study concluded that the noise correlation is negligible, and that each crystal has an independent noise source. The two crystals with the highest correlation below 8 MHz were number 2 and 10, and the corresponding correlation as a function of the frequency is shown in Fig. 9.28. It can be seen that the correlation is, on average, very small in the region of interest.

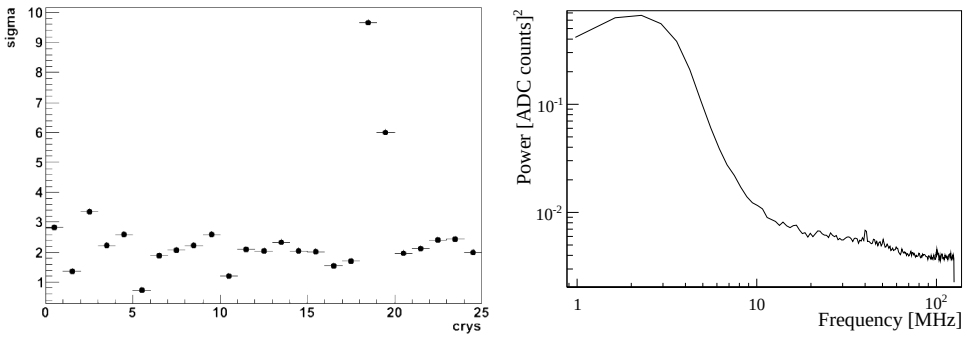

Figure 9.27: Left: Noise RMS for each channel of the BTF test beam. Right: power spectrum of a representative channel.

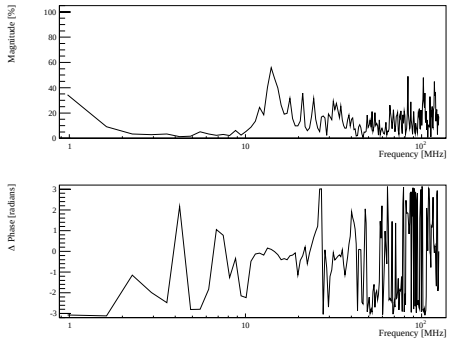

Figure 9.28: Correlation between crystals 2 and 10 as a function of the frequency. The phase takes random values when the magnitude is zero, when this happens its value should not be considered.

9.3.11.5 Temperature corrections

A temperature dependence of several percent per degree is expected both in the light yield of the LYSO crystals and in the gain of the APDs. At the CERN test beam the position of the MIP peak as a function of the temperature measured by sensors places on the rear of the crystals has been used to extract the temperature correction (Fig. 9.29) : $E_{corr} = E_{raw}/(1 - p_0 * (T - T_0))$ where $p_0 = 2.8 \pm 0.2 \times 10^{-3}$ and $T_0 = 34$K. The same figure shows also the effect of the correction.

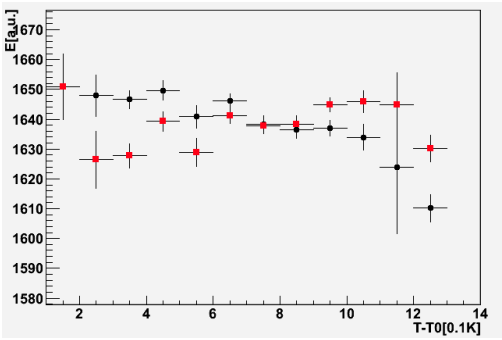

Figure 9.29: Dependence of the measured energy on the temperature before (black dots) and after (red squares) correction.

This correction proved irrelevant at the BTF test beam where the temperature was controlled to better than 0.2^oC

9.3.11.6 Algorithms and results

Two test beam have been performed with the prototype matrix of the electromagnetic LYSO calorimeter. One at CERN in October 2010 and one at the Beam Test Facility in Frascati (BTF) in May 2011. The matrix is described in detail at he beginning of this chapter. Here we are going to present the anlysis of the data collected during the two tests and the obtained results, we recall only that at the beam test at CERN 5 of the 25 crystals were equipped with PiN diodes ad photodetectors, while at the BTF all the crystals had APD's as readout.
First of all the total energy deposited in the matrix has been calculated starting from the amplitude of the digitized signal, infact it is possible to write:

$$E_{tot} = K \sum_{i=1}^{25} c_i P_i. \qquad (9.9)$$

where i is the crystal index, P_i is the amplitude of the signal, c_i are the inter-calibration coefficients, to account for differencies between channels due to different light output of the crystals or to a different electronics response and K is the conversion factor between ADC counts and the energy in MeV. Then inter-calibration coefficients for the 25 channels have been calculated using special data taking runs taken collecting data with the beam pointing at the center of each crystal. For each run events with Minimum Ionising Particle (MIP), depositing energy in only one crystal, are selected. The expected energy distribution for a MIP is a Landau one, therefore inter-calibration coefficients are calculated as the ratio between the Landau peak for each crystals and the peak of the same distribution for a crystal taken as reference, which is usually the one placed in the center of the matrix. MIP deposited energies are corrected by a factor taking into account differences in the APD gain to to temperature variation. This is measured by 5 temperature sensors put on crystals and the realitve change in APD response as a function of the temperature has found to be -2.8%. MIP events are also used to calculate the conversion factor between ADC count and energy in MeV. Energy deposited in one

LYSO crystal 20 cm long by a 1 GeV pion can be calculated using the Bethe-Bloch formula knowing the density, the mean charge, the mean atomic number and the ionization potential of the LYSO. $dE/dx = 9.72\ MeV/cm$ is found for a 1 GeV pion and the corresponding deposited energy in 20 cm is 194.3 MeV.

9.3.12 Alternatives

9.3.12.1 Full LYSO calorimeter

A possible option it to use only LYSO crystals in the whole calorimeter. Under this option the geometry of the crystals can be improved to optimize the resolution. This implies designing a new mechanical structure, with all the rest of the properties being the ones described in the sections describing the baseline option. This section summarizes such design.

The calorimeter is designed to measure with maximum precision the energy deposited by impinging particles into the crystals. All material out of the crystals is unwelcome because it absorbs a fraction of undetected (unmeasured) energy. Material in front (support shell) and between (cell walls) crystals has to be minimized. Building materials with low-Z molecular composition in limited quantities is favored for this reason. The basic physical requirement to the design of this structure is to ensure a nominal distance between crystal faces of 0.4 mm within a module (gap) and a nominal distance between crystal faces across two modules of 0.6 mm (crack). Finally, crystals should point to the interaction region.

To simplify the design we can exploit both the symmetry in ϕ and the possibility to group the crystals in four rings in theta (see Fig. 9.30 left) each composed of 36,42,48, and 54 modules respectively. The cells, whose dimensions are reported in Fig. 9.31, are designed in order to keep the cell front dimension (B, see Fig. 9.30 right).

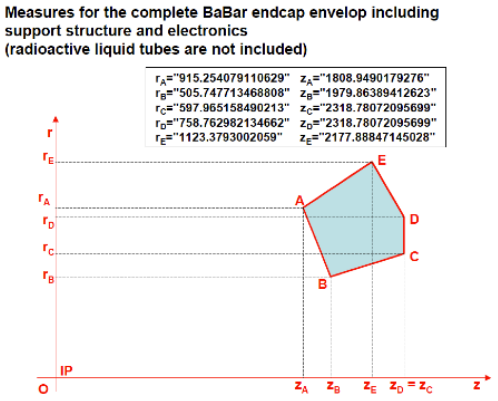

Figure 9.32: FWD EMC envelope.

General contraints and requirements

The EMC forward volume envelope is the one defined by the Babar experiment and reported in Fig. 9.3.12.1. Additional constraints coming from the new requirements for services and access have been considered.

The design of the mechanical structure foresees that the volume devoted to the EMC is divided in two, an alveolar volume and a service volume (see Fig. 9.3.12.1). The definition of this two volumes is based on assembly constraints and is optimized to simplify access to the services. Volumes shape and dimensions are such to allow free insertion of outer row of crystals.

Cooling and Calibration requirements

Structural integrity requires any produced heat to be evacuated by a cooling system. As

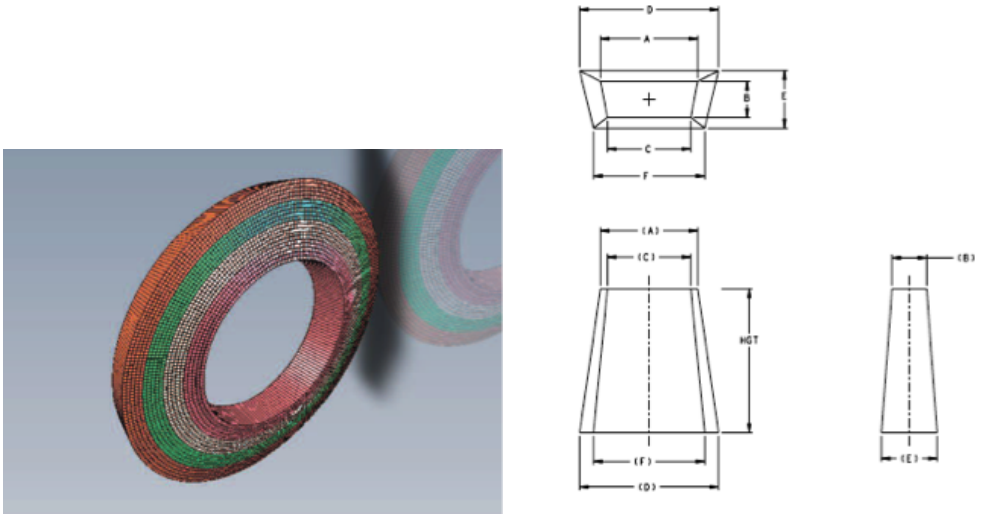

Figure 9.30: Left: overview of the structure of the FWD EMC. Right: definition of the sides of the crystals.

Ring	A	B	C	D	E	F	Front radius	Front Z	Back radius	Back Z	Angle	Crystals/Ring	Modules/Ring
1	17,99	21,38	17,27	19,9	23,84	19,1	516,5027	1977,9057	570,1961	2170,5634	15,57	180	36
2	18,69	21,41	17,98	20,69	23,88	19,89	536,7307	1969,3528	592,7885	2161,336	16,28	180	36
3	19,4	21,44	18,68	21,48	23,91	20,68	556,9553	1960,8002	615,3755	2152,0777	16,98	180	36
4	20,1	21,46	19,39	22,27	23,94	21,47	577,1766	1952,248	637,956	2142,789	17,69	180	36
5	20,81	21,48	20,1	23,05	23,96	22,26	597,3946	1943,6962	660,5288	2133,47	18,4	180	36
6	18,39	21,5	17,78	20,38	23,98	19,7	617,7018	1935,1066	683,1854	2124,0826	19,11	210	42
7	18,99	21,51	18,38	21,05	24	20,38	637,9132	1926,5562	705,7396	2114,704	19,82	210	42
8	19,59	21,52	18,99	21,73	24,01	21,05	658,1213	1918,0067	728,2829	2105,2962	20,54	210	42
9	20,2	21,53	19,59	22,4	24,02	21,73	678,3261	1909,4581	750,814	2095,8595	21,25	210	42
10	20,8	21,53	20,2	23,07	24,02	22,4	698,5278	1900,9106	773,3321	2086,3946	21,96	210	42
11	18,68	21,53	18,16	20,73	24,02	20,15	718,8334	1892,3616	795,9432	2076,8991	22,68	240	48
12	19,21	21,53	18,69	21,32	24,02	20,74	739,1376	1884,0674	818,5408	2067,6297	23,39	240	48
13	19,74	21,53	19,22	21,91	24,02	21,33	759,4449	1875,7717	841,1283	2058,3307	24,11	240	48
14	20,27	21,52	19,76	22,5	24,01	21,93	779,7553	1867,4744	863,7047	2049,0026	24,82	240	48
15	20,8	21,51	20,29	23,08	23,99	22,52	800,0686	1859,1756	886,2689	2039,6458	25,53	240	48
16	18,9	20,52	18,47	20,98	23	20,5	820,0635	1851,1039	908,4988	2030,4895	26,24	270	54
17	19,35	20,5	18,92	21,48	22,98	21,01	839,5277	1843,2795	930,181	2021,5545	26,95	270	54
18	19,8	20,48	19,38	21,99	22,95	21,51	858,9945	1835,4532	951,8474	2012,5925	27,66	270	54
19	20,25	20,45	19,83	22,49	22,92	22,02	878,4639	1827,6249	973,497	2003,6042	28,37	270	54
20	20,7	20,43	20,29	22,99	22,89	22,52	897,9357	1819,7946	995,1289	1994,5901	29,08	270	54

Figure 9.31: Nominal dimensions of the sides of the crystals. See Fig. 9.30 for the definition of the sides.

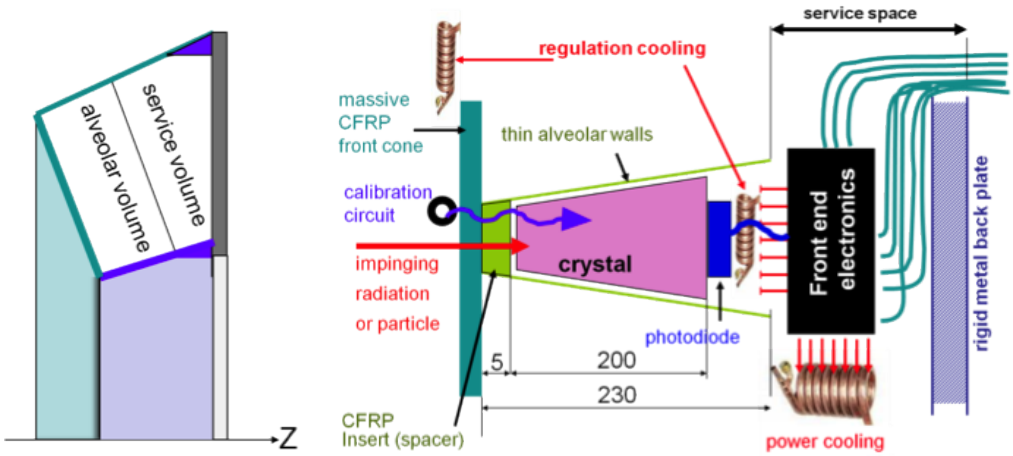

Figure 9.33: FWD EMC volumes and layout

discussed in Sec. 9.3.8 the light / signal conversion factor of the photo-detector (APD) depends on the temperature and requires a thermal regulation. There are two separate thermal volumes: the volume which encloses the crystals and photodetector, where no power dissipation is expected, and the volume comprised between the modules and the backplate, where all the thermal power is dissipated. The cooling is ensured by two active systems. A regulated circuit keeps the operating temperature of the crystal array and of the photodetector within a tight temperature spread ($\pm 0.5^o$C in BaBar). A second cooling circuit evacuates the heat generated by all power sources (front-end electronics) in the space between the modules and the back plate.

A calibration circuit flows a fluid (Fluorinert FC77) activated by a neutron source (see Sec. 9.2.7). The circuit flows past the ECAL front face, thus showering every crystal with calibrated 6,13 MeV γs, with the system shown in Fig 9.34. Under study either the possibility to reuse the BaBar monitoring system or to build a new circuit embedded in the front sandwich plate of the shell structure.

Figure 9.34: calibration circuit at the front of BaBar calorimeter

Crystal sub-unit design

The crystal subunit consists of the crystal and the capsule assembly with the photo-detector. Upon delivery crystals are visually inspected,

measured and characterized. The crystal tolerance (0.1 mm), the chamfer width (0.7 mm maximum). Crystal chamfers are necessary to ease surface lapping and polishing, avoid edge chipping and ease safe handling, match cell corner radii. Chamfer size has to be small enough to neglect the resulting light losses and maximize photo device interface (e.g. 0.3 - 0.7mm).

Module design

Modules contain a 5 x 5 matrix of crystals and therefore their approximated dimensions are 110 x 110 x 230 mm^3 and the total weight of the crystals is about 25kg. The requirements on the thickness and the material of the walls constrain the module to be held in a very light container of 220g, thus making the mechanical requirements challenging.

Physical constraints

As detailed in Sec. **??**, modules are assembled in 4 concentric rings containing growing numbers of 5x5 modules. With the ϕ and θ symmetries the number of crystals types that need to be produced is reduced to 20. To achieve the required energy resolution, crystal-to-crystal separation must be less than or equal to half a millimeter. The design guarantees a maximum distance between crystal faces of 0.4 mm within a module and of 0.6 mm across two modules, either in ϕ or in θ for crystal nominal dimensions. For the crystals with the smallest tolerances these values are reduced by 0.1 mm . Inside a module, this distance results from the following contributions (see Fig. 9.35):

- the crystal processing tolerance, from 0 to 0.1 mm.
- a guaranteed air gap between the crystal nominal (maximal) shape and the alveolar container of 0.1 mm to cope with the maximal alveolar unit elastic deformation in the worst case (crystals horizontal) and handling, transport or installation acceleration. Crystals do not take part in the structural resistance of the alveoli.
- the alveolar unit nominal wall thickness of 0.2 mm (including its manufacturing tolerance of 20 ?m). Between two modules, this distance results from the following contributions:
- the crystal processing tolerance from 0 to 0.1 mm,
- the 0.1 mm air gap inside the alveolar unit,
- the two facing walls of 0.1 mm each,
- an additional contribution of 0.35 mm due to the module copper shielding
- the 0.1mm gap between the two modules

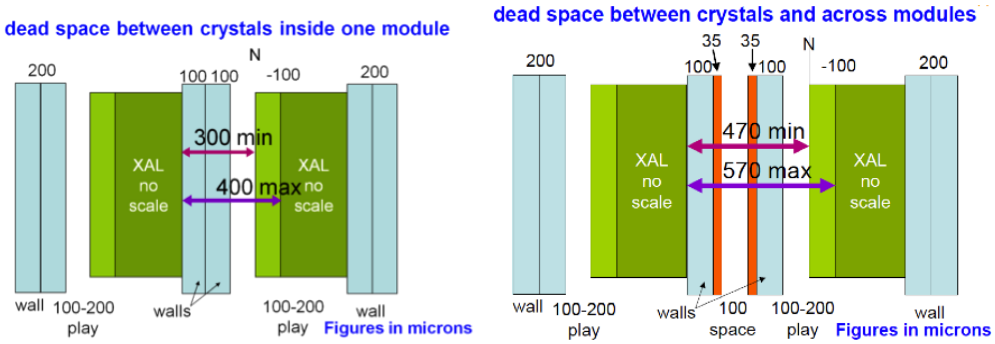

Figure 9.35: crack (crystal to crystal, left picture) and gap (module to module, right picture)

Space is left between modules to make the assembly possible (module dimensional tolerances) for module-to-module mechanical connection insertion of pre-preg fillers

The 5 x 5 modularity is considered an economic optimum (moulding cycle, handling, assembly, etc.) for the production aspects. It is also convenient for general architecture and integration front-end electronics modularity and connection and electromagnetic shielding. A 5x5 data matrices are also used in event reconstruction. A small chamfer on the crystal edges is required because of the fragility of crystals and allows a small inner radius on the cell inside. This chamfer is also very useful for the polishing process.

At the front of the crystal the cell is closed by an insert (see Fig 9.36). The inserts are made of a CFRP with short C fibers in an epoxy matrix. This material is easy to machine and a good match for the insert complex shape. Although more expensive, carbon is preferred to glass as making less material in front of the crystal. It also ensures the electrical continuity with the Cu foil of the module electromagnetic shielding. The insert has a central hole used during alveola production. Few of these holes are used for the final module positioning in the Shell-Module and for the mechanical interface through composite set-pins.

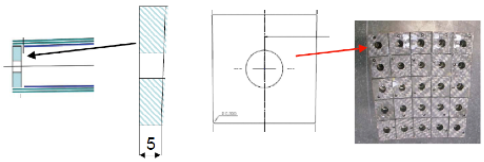

Figure 9.36: CFRP inserts at the front of the alveolar cells

At the opposite side metallic clamps tightened on cell walls keep crystals in position (see Fig 9.37).

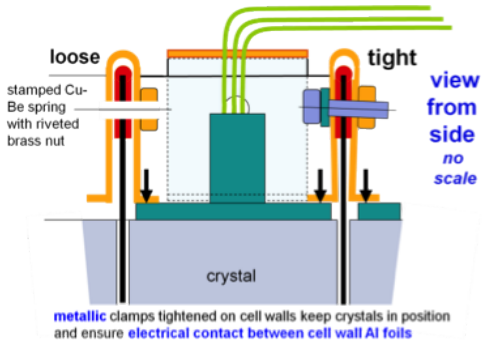

Figure 9.37: metallic clamps hold crystals in position

Grounding and shielding

An aluminum foil inside the cell acts as a reflector for the crystal and provides electromagnetic shielding. The aluminum surface can be optically improved by a special metallic or transparent coating to enhance its reflectivity. Alveolar design must allow electrical contact between all conductive materials the Al reflecting foils of every cell in one alveolar should be electrically connected. Connections are in the cell rear empty space (see Fig 9.38), through holes designed for crystal fixation.

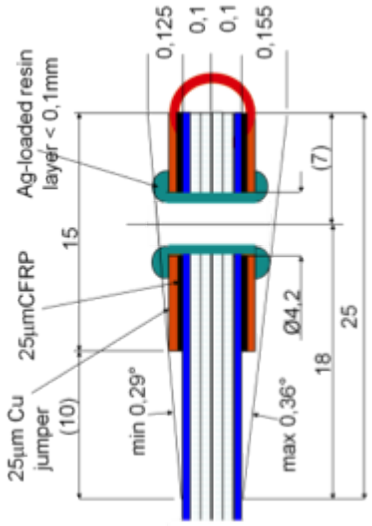

Figure 9.38: detail of the cell back open side

Cell grounding just requires to put all cell Al reflectors in contact. Cell shielding needs additional metal thickness. Alveolar shielding is achieved by an ultimate Cu wrap of 50μm around sides on the external of the module (see Fig 9.39). The Cu foil does not need additional adhesive film thickness as it is cured with the wall prepreg. The price to pay is 100μm more dead space at every module to module transition. A similar foil is merged into the Support Shell bottom plate. The bonded Cu foil, covering the four sides of the alveolar module, is connected to the cell ground.

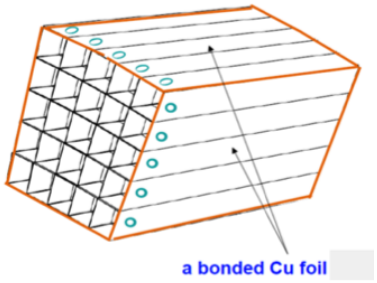

Figure 9.39: Cu foil around the module

Module supporting principles

As described in Fig 9.3.12.1 Alveolar modules are assembled into the Shell-Support-Structure (horse collar and wedge). Alveolar front ends are driven into position by 5 tubular CFRP setpins and the front of the module is glued to the structure front plate.

Alveolar back end sides are glued together via composite in θ. Connection between modules at the back reduces the bending moment of the alveola. Narrow glue strips are used because gluing of complete adjacent module walls is technically impossible. To achieve autoclave gluing of all modules in one operation the resin used for module front and sides has a lower curing temperature than that of the shell and modules. Alveolar unit moulding technique, precision, wall composition, radii and chamfers The alveolar container of a module is moulded in a precision CNC machined aluminium mould (tolerance of 0.02 mm) consisting of a box and a cover, and 25 mandrels (Fig 9.41) with shapes similar to those of crystals.

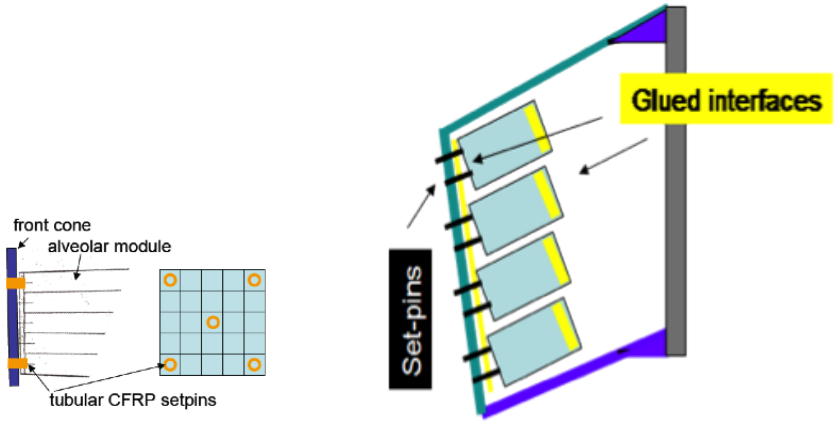

Figure 9.40: Alveola supports

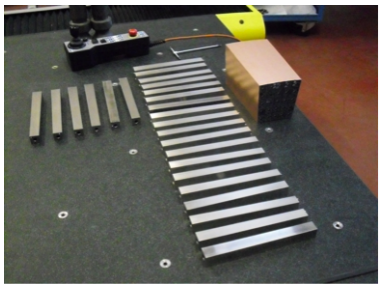

Figure 9.41: Alveolar module mandrels

The wall layers described next are wrapped around the mandrels. The mandrels are positioned with accurate setpins in precision holes of the mould box. A 50μm Cu layer is wrapped all around the module before closing the mould. Closing the mould cover presses the layers together and keeps the mandrels position with high accuracy. The moulding method requires a very uniform distance between the mandrels and the mould cavity in order to balance the very high pressures exerted when closing the mould and curing the resin. This is achieved by giving the mandrel the crystal theoretical shape increased by 0.1 mm (clearance between crystal and alveolar cavity).

The assembly (Fig 9.42) is taken to the autoclave to cure the resin. This curing is performed at 120 for 90 minutes, plus the time to reach the curing temperature and to cool down. A finishing of the ends of the module is performed after the extraction of the mandrels.

The wall of the alveola is described in Fig. 9.43. The first layer consists of an aluminium foil of a thickness of 25 μm and has a triple function. It rigidifies the alveolar unit, acts as a reflector for the crystal and provides electromagnetic shielding. The aluminum surface can be optically improved by a special metallic or transparent coating to enhance its reflectivity. The second layer consists of a glass fibre epoxy resin prepreg of a thickness of 75 μm. The 75 microns is obtained by the wrapping of two layers, 35 microns, of FGRP (Fiber Glass Reinforced Plastic). This material has been selected for its ability to produce very thin walls with a very small radius of curvature. Given wall thickness and radius limit, the combination of fibre material and diameter is such to avoid edge breaking at moulding and ensure cell structure integrity.Glass fibre is also very economical and easy to process. The 0.02 mm accuracy of the moulding is consistent with the alveolar unit tolerances. The total thickness of glass fibre wrapped around a mandrel is nominally 100 microns. The resulting surface density of material between two crystals is 200 g/m2. No other material can produce walls thin enough to maintain the gap between crystals to 0.4 mm. Compared to carbon-fibre, glass fibre has a relatively low elasticity modulus and can be formed with a sharper bending radius. Mandrels producing the inner shape are chamfered at 0.3 mm ? 45.

Module Prototypes

To validate the submodule design, two prototypes of the alveola module have been constructed (see the photos in Fig. 9.43).

A first prototype (Proto1) was produced to validate the cell structure concept and the production economy It was then used with its 25 crystals in a beam of particles for physics validation The Proto1 validated the whole production process and a 3D dimensional inspection performed on the internal and external walls gave evidence of the achievable dimensional tolerances. Wall thickness was measured at the cell open edge over 20mm depth on both sides of punched holes and produced the following values : a) for internal walls nominal 0,200mm 0,15 to 0,22 b) for external walls nominal 0,135mm 0,13 to 0,17

The information gathered have been used to define the production protocol.

Figure 9.42: alveolar module production process

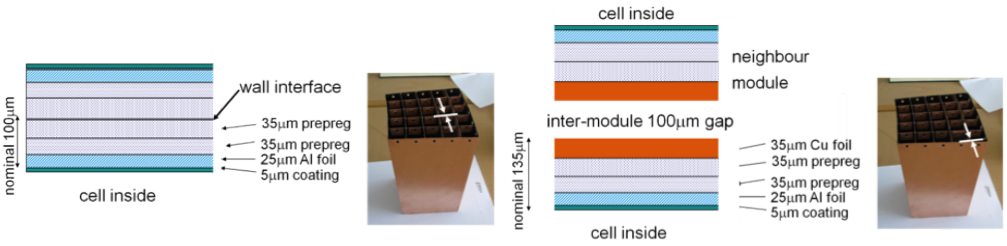

Figure 9.43: Alveolar module walls internal and external

A second prototype (Proto2) was produced in September 2011 to confirm process repeatability and to evaluate the global mechanical properties of the structure.The alveolar module is identical to that used for the physics beam test in October 2010, Proto1. The test campaign had the aim to evaluate the structure overall mechanical properties. Global deformations of the alveolar array are significant, and a loading test is essential for checking the absence of interference with the shell inside (inner and outer cone) and the absence of crystal stressing (cell bending ¡ play) in a first approximation. As shown in Fig. 9.44, the cells were loaded with dummy crystals that simulate the mass and different gravity vectors have been investigated. The mechanical tests performed on the modular structure provided basic input data to a Finite Element Analysis of the complete support structure.

Alveolar module structure finite element analysis

A detailed Finite Element Analysis was performed on the alveolar structure using material properties form data-sheet. The analysis predictions have been compared with the outcome of the load test on Proto2 and the model tuned to best fit the real behaviour. This detailed model, shown in Fig. 9.45, has been used as reference to to validate the Global Finite element model of the whole EMC.

Support shell structure design

The shell, shown in Fig. 9.46, consists of the outer cone and front cone as one single solid body in CFRP. The inner cone, where material budget does not pose too stringent limits is a metallic shell. Back plate is the same as BaBar. The volume is defined by the line AB, AD, CD while A'B' and A'D' are construction lines resulting from technical choice.

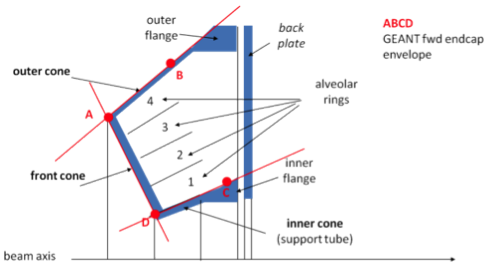

Figure 9.46: Support shell structure

The outer cone end is reinforced by a metallic ring for easy connection with the back plate. The back plate provides the EMC interface with the SuperB bearing points (position reference and transmission of loads). The alveolar array is cantilevered from the shell front cone as detailed in Fig. 9.47.

This configuration provides a logical construction and assembly sequence, in particular an easier and almost reversible access to the most delicate part of the detector, its crystals and photodiodes. There is no connection between the alveolar array and the inner and outer cone inner faces. A 1mm gap is introduced for the free elastic deformations of the alveolar array and of the shell. The front cone is connected to the inner cone by gluing secured by screws.

Support Shell unit production and materials

The outer cone is a massive CFRP (6 to 10mm) while the front cone is either a massive CFRP or a sandwich plate 20mm thick. For the production the mould is at the inner face of the outer-front cone in order to have high dimensional accuracy at the interface with the crystals modules, while a vacuum bag is at the

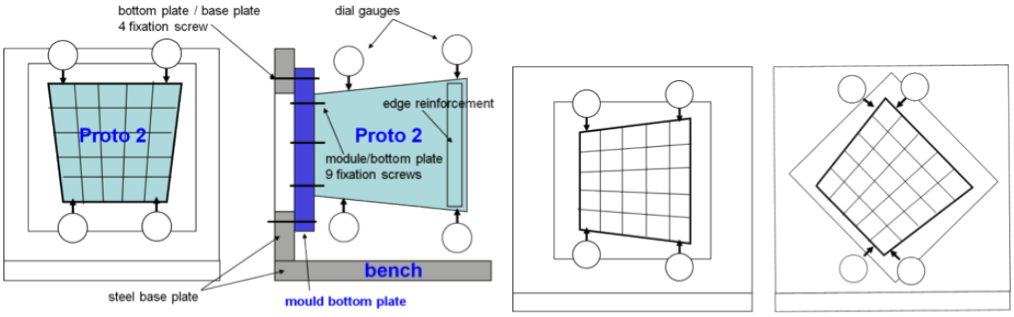

Figure 9.44: alveolar module test setup

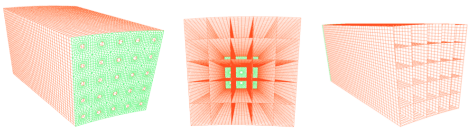

Figure 9.45: Alveolar module finite element model

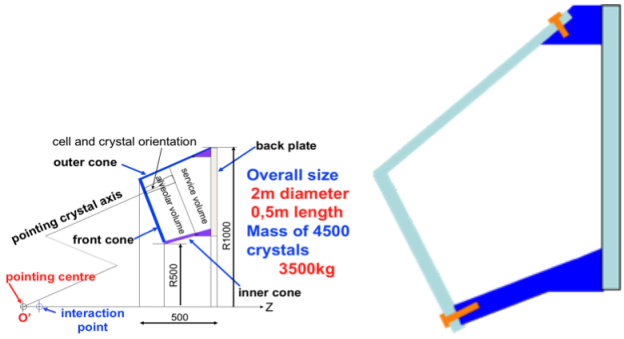

Figure 9.47: Suppert shell assembly

opposite side; the parietal aluminum wedge is embedded in the structure The inner cone is a precise CNC machined massive Al 7075 piece with a thickness of 20mm.

Global structure finite element analysis

To the front conical plate are connected 180 alveolar modules (of 5 x 5 cells) of four different types, displayed in four concentric rings. Because of the circular configuration each module is in a different loading case. The resulting FE model of the complete distribution of alveolar modules supported by the shell structure would result in a large size, . An alternative parallel solution was followed to reduce the alveolar module to its main useful parameters (superelements) that do not contain all the geometrical detail but that closely characterize the mechanical behavior of the alveola. The input mechanical properties used for the superelements come from the mechanical tests performed on the Proto2.

9.3.12.2 Pure CsI

Description

Performance, tests

Mechanical changes

Electronics changes

9.3.12.3 BGO

Prior experiences with calorimeters made of BGO crystals in high energy physics come from L3 [**?**] and Belle [**?**]. In the first case BGO was used for both Barrel and Endcaps, while Belle used BGO to build the Extreme Forward Calorimeter with the purpose of improving hermeticity close to the beam line and monitor beam background. Such knowledge will be summarized here, integrated by tests that were performed to account for the particular operating conditions expected in the case of SuperB: short integration time, needed to reduce pile-up, and large radiation.

Resolution

The properties of the BGO crystals are summarized in Tab. 9.2: mechanical properties similar to LYSO, but with a light yield four times smaller. The scintillation time is intermediate between the LYSO and the CsI, reason for which a good performance in a high rate environment is expected.

The performances of the L3 calorimeter, read by pin-diodes were $\sigma_E/E = (1.6/\sqrt{(}E)\oplus 0.35)\%$ and $\sigma_\theta = ((6/\sqrt{(}E) \oplus 0.3)mrad)$, i.e. the statistical term of the resolution at 100MeV was 4%. Later studies with APDs [**?**] show that the system produces $\sim$ 420 p.e./MeV, i.e. the statistical term at 100 MeV would be 0.5%, i.e. well within the requirements.

Nonetheless, due to the requirements dictated by machine background (Sec. **??**) we will not be able to operate the detector integrating over even as much as a decay time of the crystal. The degradation in resolution induced by the integration time will have to be tested specifically for this application.

LAB TESTS

Radiation Hardness

The BGO rad-hardness was tested up to 90Mrad [**?**, **?**]. After a drop of about 30% in the first 20Mrad of integrated dose the crystal light

yield plateaus. It will nonetheless recover up to 90% of the original light yield in approximately 10 hours and it is not documented what will happen if after this pre-irradiation the crystal receives a small dose further. For non irradiated crystals a dose of 115krad implies a light yield loss of 30% that fully recovers with a lifetime of $\sim$ 1 hour. Furthermore, these results refer to undoped, recently produced crystals, but they depend strongly on the level of doping and the manifacturer.

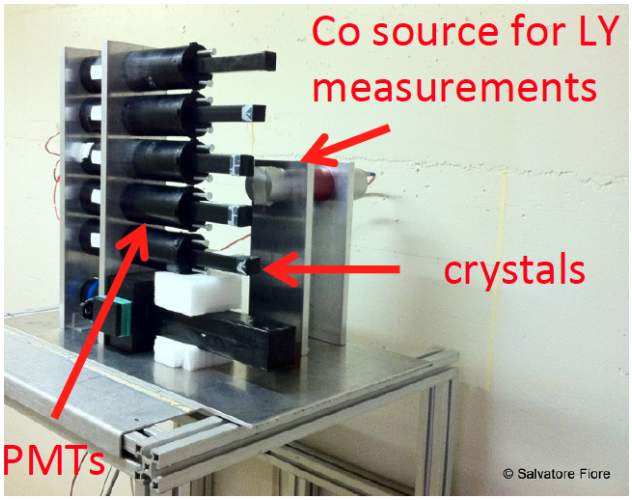

Figure 9.48: Experimental set-up for LY measurements. Crystal samples are shown while mounted on the PMTs. Crystals were coupled to the PMTs during low-dose irradiation, and data were acquired by shutting down the source for few minutes.

To customize the radiation hardness study to our case, we exposed four samples of BGO crystals to γ-rays from a high-activity ^{60}Co radioactive source. Two crystals of 2.2x2.2x18 cm^3 have been previously used in the L3 experiment at CERN, other two crystals of 2.5x2.5x20 cm^3 were recently supplied by the Shanghai Institute of Ceramics (SIC).

Irradiations and measurements took place at the Calliope Gamma Irradiation Facility at ENEA-Casaccia center (Rome). The irradiation source is a cylindrical array of ^{60}Co source rods emitting γ-rays of 1.1 and 1.3 MeV, in an irradiation cell of 6x7x3.9 m^3 plus an attached gangway. Depending on the placement of the samples, dose rates from few rad/h up to 230 krad/h are available. The source can be moved outside or inside its shielding pool in less than two minutes.

Plastic mechanical supports for the crystals, not shielding them from the radiation, allowed us to expose the samples to different dose rates, and to couple them to EMI 9814B Photomultiplier Tubes (PMT) to perform the LY measurements using a low-activity ^{60}Co calibration source. PMTs were read out by a CAEN VME ADC.

We started our irradiation campaign by exposing the crystals to 5-10 rad/h dose rate for few hours. We were able to measure the LY once every 20 minutes of irradiation, with only two minutes delay after the source was shut down. Using this approach we measured the progressive LY reduction at different dose rates. We measured the LY recovery after 15-30 rad and 170 rad doses, and evaluated the recovery time constant for the different samples. The LY recovery curve has been fit with an exponential function, yielding a time constant of (2.7$\pm$0.4) h for 15 rad dose and (4.5$\pm$0.2) h for 170 rad dose.

We then exposed some crystals to a massive dose rate of 230 krad/h for a total dose of 12 Mrad, and then to small doses with 1.5 rad/h

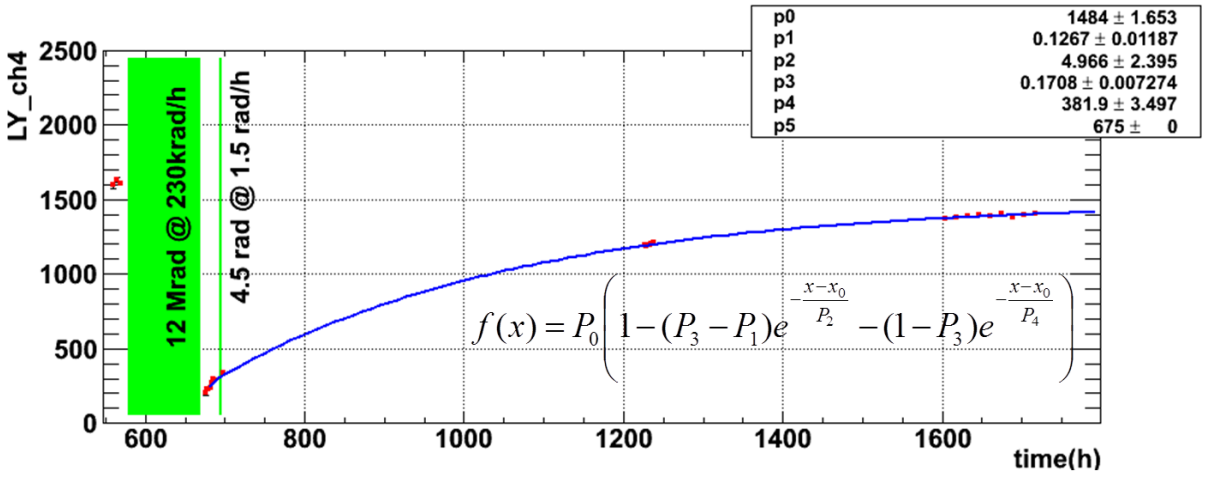

Figure 9.49: LY measurements with respect to time, after one massive irradiation of 12 Mrad. A two-component exponential recovery function fits the experimental data. A 3h irradiation at 1.5 rad/h does not affect the LY recovery.

rate, to measure the sensitivity to small dose rates after strong delivered doses. We measured LY reductions up to 1/5 of the pre-irradiation LY value. A long-term recovery was then analized and exploited to measure the recovery time constant. We fit the LY recovery data with a double-exponential function, yeldind a short time constant of (5.0±2.4) h and a long time constant of (381.9±3.5) h . BGO crystals from L3 experiment showed a larger damage after each irradiation, but also a faster recover capability, while crystals from SIC hardly recovered from radiation damage.

Light transmission spectra have been acquired before and after irradiations, in order to identify the nature of the LY reduction. As previously stated, the radiation-induced LY reduction could be due either to a decrease of the light transmittance, or to a damage of the scintillation mechanism itself. By comparing the LY and transmittance measurements, we observed that the main effect of the radiation damage was a reduction of the light transmission due to color-centre formation.

9.3.12.4 Comparison with baseline

Table 9.3.12.4 is a comparison of the volume and total cost of the scintillating crystals required for the forward endcap in several different configurations. The baseline design, employing LYSO crystals, contemplates complete replacement of the existing mechanical structure. A new carbon fiber aveolar and associated structure to mount the crystals on the doors of the magnet is estimated in the Super$B$ TDR to cost euro X.Y. The total cost of the endcap is the sum of the crystal production and preparation costs, the photosensor readout and associated electronics, the mechanical structure, associated cooling and electronic services and the calibration system. Thus the crystal cost is only one component, *albeit* the largest, of the system.

There are nine rings of for crystals in the existing *BABAR* CsI(Tl) endcap structure. Complete replacement of the CsI(Tl) requires 3600 LYSO or BGO crystals or 900 pure CsI crystals. Table 9.3.12.4 shows the volume of crystals required for complete replacement and the estimated costs for these crystals, but does not include the other mechanical or readout costs listed above.

The table also lists three hybrid options, in which a number of the outer CsI(Tl) rings of the endcap are retained (since they are approximately at the same distance from the interaction region as are the forward barrel crystals) and the inner rings are replaced by LYSO crystals. The retention of the existing *BABAR* mechanics is intrinsic to this option, providing a substantial additional savings. As the Moliére radius of LYSO is one half that of CsI(Tl), four LYSO crystals can be placed into one CsI(Tl) compartment. If three CsI(Tl) rings are retained, the required volume of LYSO is reduced by 40%. Including the savings in mechanics, this represents a factor of two reduction in the cost of the endcap. The volumes for replacement of four and five of the nine rings are also included in the table.

Option	Number of New Crystals	New Crystal Volume (cc)	Cos
LYSO full (baseline)	3600	330559	2
3 CsI(Tl) + 6 LYSO	2160	195590	2
4 CsI(Tl) + 5 LYSO	1760	156412	2
5 CsI(Tl) + 4 LYSO	1360	118672	2
Pure CsI	900	680140	
BGO	3600	330000	

Table 9.4: Comparison of crystal volume and crystal costs for several forward endcap configuration options.

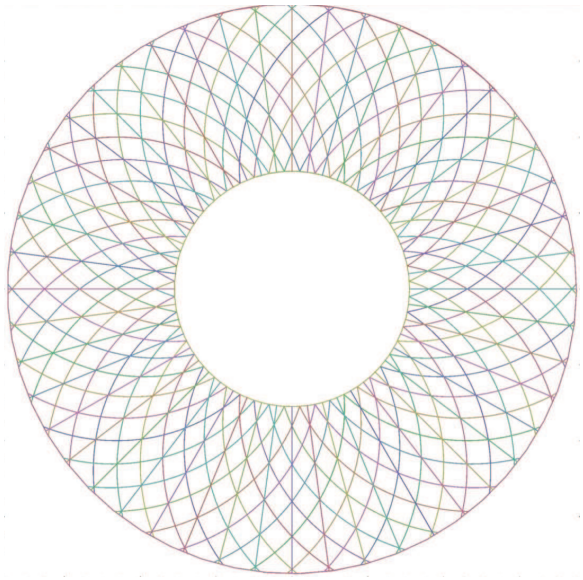

Figure 9.51: The backward EMC, showing the scintillator strip geometry for pattern recognition.

9.4 Backward Calorimeter

The backward electromagnetic calorimeter for Super$B$ is a new device with the principal intent of improving hermeticity of the detector at modest cost. Excellent energy resolution is not a requirement, since there is significant material from the drift chamber in front of it. Thus, a high-quality crystal calorimeter is not planned for the backward region. The proposed device is based on a multi-layer lead-scintillator sampling calorimeter with longitudinal segmentation providing capability for π/e and K/π separation at low momenta. The design is derived from the analog hadron calorimeter for the ILC [1].

The backward calorimeter is located behind the drift chamber starting at z= $-1320\,\mathrm{mm}$ (see Figure 9.50) allowing room for the drift chamber front end electronics. The inner radius is 310 mm, the outer radius is 750 mm and its total thickness is less than 180 mm covering $12X_0$. It is constructed from a sandwich of 2.8 mm Pb plates alternating with 3 mm plastic scintillator strips (*e.g.*, BC-404 or BC-408). The scintillation light of each strip is collected by a wavelength-shifting fiber (WLS) coupled to a photodetector located at the outer radius. The scintillator strips come in three different geometries, right-handed logarithmic spirals, left-handed logarithmic spirals and radial wedges. This pattern alternates eight times. Each layer contains 48 strips producing a total of 1152 readout channels. The strip geometry is illustrated in Fig. 9.51

The WLS fibers, Y11 fibers from Kuraray, are embedded in grooves milled into the center of the scintillator strips. Each fiber is read out at the outer radius with a $1 \times 1\,\mathrm{mm}^2$ multi-pixel photon counter (SiPM/MPPC) [7]. A mirror is glued to each fiber at the inner radius to maximize light collection. The SPIROC (SiPM Integrated Read-Out Chip) integrated circuit (IC) [8] developed for the ILC is used to amplify and digitize the SiPM/MPPC signals, providing both TDC (100 ps) and ADC (12 bit) capability. Each ASIC contains 36 channels. Since these ASICs were developed for SiPM readout, where the intrinsic gain is much higher, an additional preamplifier is coupled to the SiPM/MPPCs. This has the advantage to place the SPIROC ASICs at a convenient place in the detector without introducing additional noise.

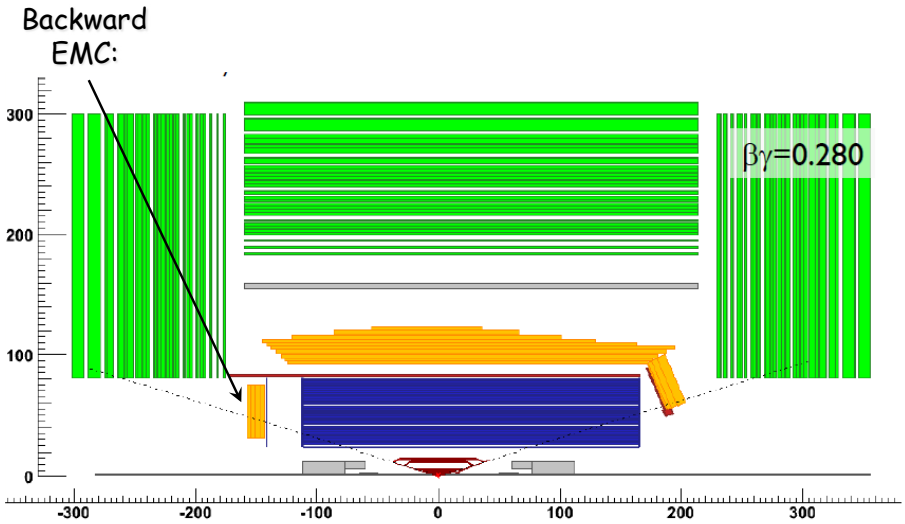

Figure 9.50: Layout of the calorimeters in the SuperB detector.

9.4.1 Improvements on physics results

9.4.2 Requirements

The main goal of the backward EMC is to increase the calorimeter coverage by recording any charged or neutral particle in the backward region. This information is important in particular for analyses that utilize the recoil method with hadronic and semileptonic tags to select B meson decays with neutrinos in the final state. The backward EMC helps to increase the selection efficiency and to improve background rejection. For this task, excellent energy resolution is not necessary. It is more important to keep the costs moderate. With moderate energy resolution and good angular resolution π^0 reconstruction is anticipated. Furthermore, the backward EMC has the capability to measure time-of-flight and the energy loss via ionization of charged particle well. This information is very useful for particle identification, in particular π/e and K/π separation at low momenta.

9.4.2.1 Energy and angular resolution

Since the backward EMC prototype is still in the construction phase, presently no results on energy resolution and angular resolution exist. However, electromagnetic sampling calorimeter prototypes with plastic scintillator strips and tiles have been tested in test beams within the CALICE collaboration [9]. The energy resolution for the stochastic term is $15\%\sqrt{E}$ and for the constant term is around 1%. For the CALICE analog hadron calorimeter which has a non-optimized geometry for electromagnetic showers, the stochastic term was measured to be around $20\%/\sqrt{E}$. For low photon energies, an additional noise term of $\sim 130\,\mathrm{MeV}/E$ contributes. Thus, the backward endcap EMC is expected to have a similar performance with a stochastic term of $15 - 20\%/\sqrt{E}$.

The left-handed logarithmic spirals are defined by

$$x(t) = r \exp b \cdot t \cos t - r \tag{9.10}$$

$$y(t) = r \exp b \cdot t \sin t \tag{9.11}$$

$$\tag{9.12}$$

For $r = r_o/2 = 37.5\ cm$ and $b = 0.2$ eight left-handed spiral strips overlap with eight right-handed spiral strips defining a specific tile-shaped region. The radial strips overlap with five left-handed (right-handed) spiral strips. In the worst case, the resolution is $\sigma_r = \sigma_\phi \simeq 29\,\mathrm{mm}$ for a single tile in the outer region. This is improved to $\sigma_r = \sigma_\phi \simeq 12\,\mathrm{mm}$ in the inner region. If the shower is distributed over several adjacent tiles, its position can be determined by the center-of-gravity method improving the position resolution significantly.

9.4.2.2 Background rates

Present background simulations indicate that the worst n rate in layer zero of the backward IFR end cap is 3.5 kHz/ $\mathrm{cm}^{-2}\mathrm{s}^{-1}$. The radiation profile shown in Figure 9.52 indicates that the worst rates for all energies of 3 kHz/ $\mathrm{cm}^{-2}\mathrm{s}^{-1}$ occur in the inner most region. In ten years of running this amounts to $6.1 \times 10^9\ n/\,\mathrm{mm}^2$ in the region near the inner radius. The background rates drop by significantly towards outer radius. At the the location of the photodetector, the rate is reduced by more than a factor of 10. Further simulation studies are needed, since due to the high rate at the inner radius an occupation problem may be present. To deal with this issue one either subtracts a higher average background energy from each strip or divides the strips into two segments at the cost of doubling the number of photodetectors. The former solution will have an effect on the energy resolution since the background energy deposit has a wide distribution. The latter solution is preferable, but is about $\$100k$ more expensive.

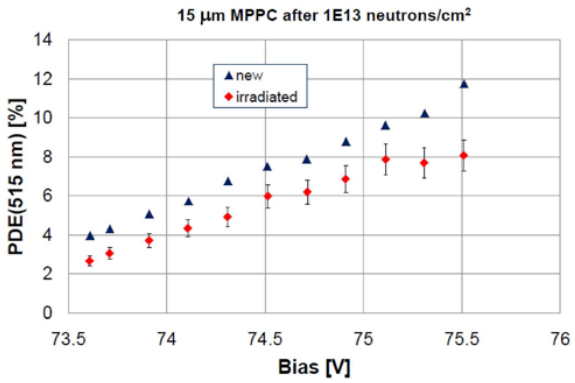

Figure 9.53: The efficiency of $15\,\mu\text{m} \times 15\,\mu\text{m}$ pixel MPPCs as a function of the bias voltage before and after irradiation with $10^{13} n/\,\text{cm}^{-2}\text{s}^{-1}$.

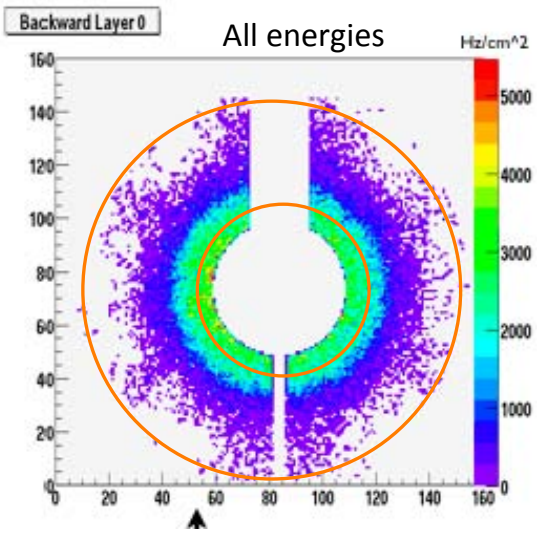

Figure 9.52: The distribution of background hits of all energies in the backward layer 0. The coverage by the backward EMC is shown by the red circles.

9.4.2.3 Radiation hardness

Irradiation of Si detectors causes the dark current to increase linearly with flux Φ:

$$\Delta I = \alpha \Phi V_{eff} G, \tag{9.13}$$

where $\alpha = 6 \times 10^{-17}\ A/\,\text{cm}$ $V_{eff} \sim 0.004\,\text{mm}^3$, Φ is the flux, V_{eff} is the bias voltage and G is the gain. Since the initial resolution of MPPCs/SiPMs of $\sim 0.15pe$ is much better than that of other Si detectors, radiation effects start at lower fluxes. For example, at a flux $\Phi = 10^{10}\ n/\,\text{cm}^{-2}\text{s}^{-1}$ the individual single pe signals are smeared out. The MIP peak is still visible at $\Phi \sim 10^{11}\ n/\,\text{cm}^{-2}\text{s}^{-1}$. The number of observed hot spots and the noise rate increase after irradiation of $3 \times 10^{9}\ n/\,\text{cm}^{-2}\text{s}^{-1}$. No significant changes are observed on the cross talk probability and no significant change on the saturation curves. The main effect is an increase in noise after exposure to high n dose. Hamamatsu has produced news SiPM/MPPCs with $20\,\mu\text{m} \times 20\,\mu\text{m}$ and $15\,\mu\text{m} \times 15\,\mu\text{m}$, which have lower detection efficiency due to more boundaries and thus need a higher bias voltage to compensate for losses. Figure 9.53 shows the detection efficiency as a function of bias voltage for $15\,\mu\text{m} \times 15\,\mu\text{m}$ detectors before and after irradiation with $10^{13}\ n/\,\text{cm}^{-2}\text{s}^{-1}$. For the new detectors, signal/noise and the equivalent noise charge look fine after irradiation. According to Eugenios study the backward endcap EMC will record $10^{11}\ n/\,\text{cm}^{-2}\text{s}^{-1}$ after 10 years operation. Thus, if the $25\,\mu\text{m} \times 25\,\mu\text{m}$ pixel SiPM/MPPC show a problem we switch to one of the new SiPM/MPPCs with smaller pixel size.

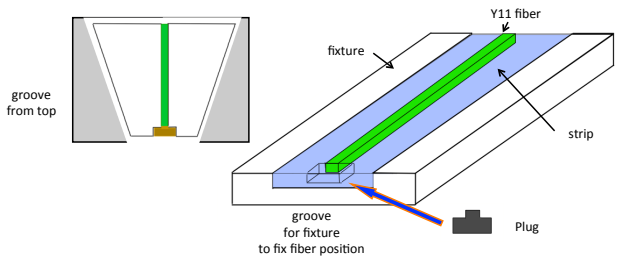

Figure 9.54: Schematic of holding the scintillator strip in a fixture for mounting the MPPC to the Y11 fiber.

9.4.2.4 Solid angle, transition to barrel

In the laboratory frame, the backward EMC covers a full polar angle region from 231 mrad to 473 mrad. Partial coverage extends the polar angle region from 209 mrad to 517 mrad. In the present design, there is a gap between the backward EMC and the barrel covering the region 517 mrad to 694 mrad in the laboratory frame. In the center-of mass frame, full coverage of the backward EMC is in the region 215 mrad to 442 mrad, while partial coverage exists in the region from 194 mrad to 482 mrad. If the backward EMC could move closer to the IR, the gap to the barrel calorimeter could be reduced.

9.4.3 Mechanical design

The 3 mm thick scintillator strips are cut individually from a scintillator plate. Thus, the plate size and the cutting procedure need to be carefully thought through to minimize the amount of waste. For the spiral strips the least waste and fastest production is obtained by fabricating a mould. However, this approach may be too expensive, since the total number of spiral strips is rather small. The preferred scintillator material is BC 404 from St Gobain, since it has the smallest decay time for TOF capability and its emission spectrum is reasonably matched to the Y11 absorption spectrum. The strip width is 38 mm at the inner edge increasing to 98 mm at the outer edge. The strip sides are painted with a white diffuse reflector. Front and back faces are covered with reflectors sheets (3M, Tyvec). Test bench measurements have shown that the yield along the strips varies by more than a factor of two. To restore uniformity, a pattern of black dots is printed onto the white reflector sheets.

In the center of each strip, a 1.1 mm deep groove is milled into which the 1 mm thick Y11 WLS fiber is inserted. At the outer edge of the strip, the groove is cut 0.4 mm deeper so that the active area of the SiPM/MPPC fully covers the fiber. The SiPM/MPPC is housed in a small precisely cut pocket. Especially fabricated fixtures out of Teflon or Nylon will hold a strip. The fiber groove at the outer edge is closed with a plug at the position of the photodetector. The Y11 fiber is pressed against the plug and held with a drop of glue. After removing the plug the SiPM/MPPC is inserted and is glued onto the Y11 fiber to match refractive indices. A mirror is placed at the other end of the fiber to detect the light that moves away from the photodetector. So tolerances in the length of the Y11 fiber are picked up at the mirror end. The strip layout is shown in 9.54.

To hold the strips in each layer in place 1.5 mm deep and 1 mm wide grooves are cut into the lead plates. The shape of groove matches that of the strip. A 3 mm thick and 1 m wide and 550 mm long plastic strip is inserted into the groove and is glued. This structure is strong

enough to hold the scintillator strips in place. The calorimeter can be rotated by 90°. This is needed for operation with cosmic muons that yield a MIP calibration and allows for testing the calorimeter before installing it into the SuperB detector.

The entire calorimeter just weighs about 1300 Kg. An Al frame with a strong rear plate and a strong inner cylinder will hold the backward EMC in the SuperB detector. The front plate and outer cylinder needed for closure and shielding can be thin. Concerning cost and performance it is advantageous to build the backward EMC as a single unit. This requires the calorimeter to slide back on the beam pipe supported on the tunnel walls. It needs to be fixed at the tunnel and is rolled in. Since the inner radius is 31 cm, there is sufficient clearance for pumps and other beam elements. The design of this capability requires a detailed drawing of the beam pipe and the position and size of machine elements.

It is possible, however, to build the backward EMC in two halves with a vertical split. The impact of such a design is that ten strips per layer have to be cut into two segments. The inner segments of these strips have to be read out at the inner radius. This increases the number of channels by 240, requiring 240 additional SiPM/MPPCs, seven extra SPIROC boards and four extra calibration boards. This layout will deteriorate the performance near the vertical boundary. The effect needs to be studied in simulations. This certainly adds extra costs at the order of $\sim 20\%$.

9.4.3.1 Calorimeter construction

Each completed strip with Y11 fiber and MPPC mounted is tested in the lab with a ^{106}Ru source. All important properties, such as bias voltage, gain, noise, and MIP position are recorded in a data base. Stacking will start from the rear to the front. The rear Al plate rotated by 90° is placed on the mounting table and the inner cylinder is bolted on to it. The back plate requires 48 radially milled grooves into which the plastic strips are inserted that will hold the scintillator strips. Next, all scintillator strips are mounted, the MPPCs are connected to preamplifiers and a Pb plate with right-handed logarithmic spiral grooves is placed on top completing layer 24. This procedure is repeated 24 times. Finally, another scintillator layer with radial strips and the front plate are stacked. The scintillator layer 0 yields information on the shower origin.

Before the outer cylinder is bolted on, temperature sensors and clear fibers need to be installed at the outer ring that transport light from a UV LED to the strips. If each fiber illuminates 13 strips via a notch spaced equidistantly every 12 mm, a total 96 fibers are sufficient. The fibers run through small holes in the back plate from the rear to the front. Attaching four fibers per LED, 24 LEDs housed outside the rear plate are needed.

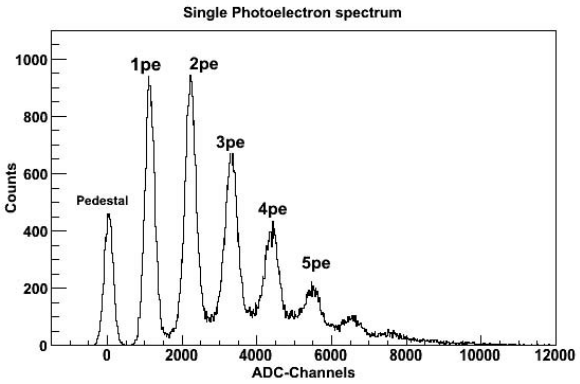

Figure 9.55: Single photoelectron spectrum measured with a Hamamatsu S10362-11-025P MPPC.

9.4.3.2 Support and services

The preferred option is to build the backward EMC as one unit. In order to avoid breaking the beam pipe when access is required to the drift chamber endplate, the backward EMC must be be able to slide back far enough. The explicit design requires a detailed design of the IR with all machine elements in place. In the detector position, the weight is supported by two brackets that are fixed at the rear endplate and on the inner wall of the IFR backward endcap. When rolling back the weight could be supported by the tunnel wall. To allow for a smooth sliding back, rolls are mounted on the inner support cylinder.

The 32 SPIROC ASICS and four calibration boards are mounted on the rear support plate of the EMC. Each SPIROC ASIC has one multiplexed USB output cable to the DAQ, a cable providing low voltage input for +5.5 V and -7.5 V, a cable for the MPPC bias voltage of 70 V, an electronic calibration input and an analog output. Since the 36 signal cables remain inside the detector, a total 192 cables have to be supplied from the outside to the SPIROC ASICs.

The four CMBs are also mounted on the rear support plate. Each CMB holds six LEDs and six PIN photodiodes and need to read out four thermocouples. Including the low voltage supplies for the CMB electronics, 80 cables are needed for the CMBs, yielding 272 cables in total.

Table 9.5: Properties of Hamamatsu MPPCs

MPPC type	# cells $1/\,\mathrm{mm}^2$	C [pF]	R_{cell} kΩ]	C_{cell} [fF]	$\tau = R_c \times C_c$ [ns]	$V_{break\ down}$ [V] at T=23 C	V_{op} [V] at T=23 C	Gain [10^5]
15 μm	4489	30	1690	6.75	11.4	72.75	76.4	2.0
20 μm	2500	31	305	12.4	3.8	73.05	75	2.0
25 μm	1600	32	301	20	6.0	72.95	74.75	2.75
50 μm	400	36	141	90	12.7	69.6	70.75	7.5

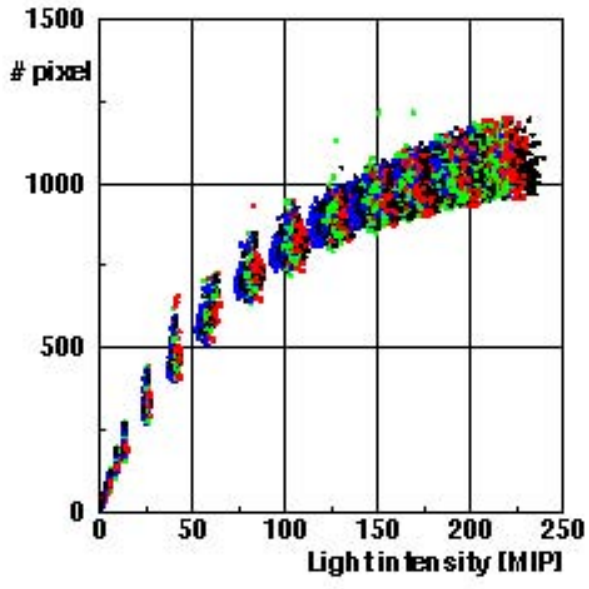

Figure 9.56: Saturation curves of 10,000 SiPMs measured in the CALICE analog hadron calorimeter.

9.4.4 SiPM/MPPC readout

The photodetectors are SiPM/MPPCs from Hamamatsu (type S10362-11-025P) with a sensitive area of 1 mm × 1 mm holding 1600 pixels with a size of 25 μm × 25 μm. These detectors are avalanche photodiodes operated in the Geiger mode with a bias voltage slightly above the breakdown corresponding to $50 - 70$ V providing a gain of a few 10^5. They are insensitive to magnetic fields. Each pixel typically has a quenching resistor of a few MΩ so they recover within 100 ns. The efficiency is of the order of $10 - 15\%$. Since the SiPM/MPPCs record single photoelectrons as shown in Fig. 9.55 for a Hamamatsu MPPC, they are auto-calibrating. SiPM/MPPCs are non-linear requiring non-linearity corrections for higher energies. As an example, Fig. 9.56 shows the response curves of 10,000 SiPMs measured at ITEP most of which were installed in the analog hadron calorimeter [1]. The dynamic range is determined by the number of pixels. Properties of several SiPM/MPPCs are listed in Table 9.5.

A concern with SiPM/MPPCs is radiation hardness. Degradation in performance is observed in studies performed for the Super B IFR, beginning at integrated doses of order 10^8 1-MeV-equivalent neutrons/ cm^2 [10]. This needs to be studied further, and possibly mitigated with shielding. Another alternative is look into a different photodetector. Recently, Hamamatsu has produced SiPM/MPPCs with pixel sizes of 20 μm × 20 μm and 15 μm × 15 μm (see Table 9.5). A CMS study shows that the performance of these new photodetector deteriorates only slightly after an irradiation of $10^{13} n/\,\mathrm{cm}^{-2}\mathrm{s}^{-1}$.

9.4.5 Electronics

The signal of the SiPM/MPPC is first amplified with a charge-sensitive preamplifier then fed into the auto-triggered, bi-gain SPIROC ASIC. The SPIROC board has 36 channels. Each channel has a variable-gain charge preamplifier, variable shaper and a 12-bit Wilkinson ADC. It allows to measure the charge Q from one photoelectron (pe) to 2000 pe and the time t with a 100 ps accurate TDC. A high-level state machine is integrated to manage all these tasks automatically and control the data transfer to the DAQ. The SPIROC ASIC was designed to supply the high voltage for the SiPM/MPPC. Using a DAC, individual high voltages within ± 5 V can be supplied to each photodetector.

The SPIROC ASIC gives Gaussian signals with no tails, shows excellent linearity and low noise. 32 ASIC readout boards are needed to read out the entire endcap. The boards are mounted in two layers behind the endcap. The first layer holds 20 boards and the second layer the remaining 12 boards. Each board connects to 36 SiPM/MPPCs via a ribbon cable that were designed for ILC at a luminosity of $\mathcal{L} = 10^{34}\ \mathrm{cm}^{-2}\mathrm{s}^{-1}$.

9.4.6 Calibration

An LED-based calibration system with fixed LED intensities is used to monitor the stability of strip-fiber-SiPM/MPPC system between MIP calibrations, to perform gain calibrations, determine intercalibration constants, and to measure the SiPM/MPPC response functions. This is necessary since the SiPM/MPPCs have a temperature and voltage dependence of the gain of

$$\frac{dG}{dT} \sim -1.7\%/\mathrm{K}, \tag{9.14}$$

$$\frac{dG}{dV} \sim 2.5\%/0.1\ \mathrm{V}. \tag{9.15}$$

The temperature and voltage dependence of measuring the charge of the scintillation signal is

$$\frac{dQ}{dT} \sim -4.5\%/\mathrm{K} \tag{9.16}$$

$$\frac{dQ}{dV} \sim 7\%/0.1\ \mathrm{V} \tag{9.17}$$

The calibration system is based on a new design for the analog hadron calorimeter. Light from a UV LED is coupled to clear fibers. The fibers are notched at equidistant positions. The shape of each notch changes such that it emits about the same intensity of light. For the backward EMC, 96 fibers with 13 notches each are sufficient to illuminate all strips. If four fibers are coupled to one LED, 24 LEDs are needed whose light is monitored by a PIN photodiode. A few thermocouples distributed throughout the outer edge of the EMC near MPPCs measure temperature. Both temperature and bias voltage are recorded regularly by a slow control system. After temperature and PIN diode correction the stability of LED system is better than 1%.

The old CMB boards are too big to be mounted at the outer radius of the EMC. However, the new calibration boards are 40 mm $\times$ 140 mm in dimension and house one LED, one PIN diode, the electronics to read out the PIN diode, monitor temperature and MPPC voltage. The boards are sufficiently small to be mounted at the backplate near the outer radius. They can be arranged such that the fibers can be nearly straight.

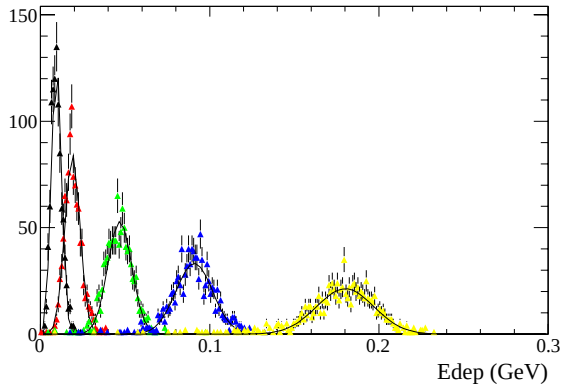

Figure 9.57: Energy depositions from mono-energetic photons (0.1 GeV, 0.2 GeV, 0.5 GeV, 1 GeV and 2 GeV) observed in the scintillators of the backward EMC generated in front of the EMC.

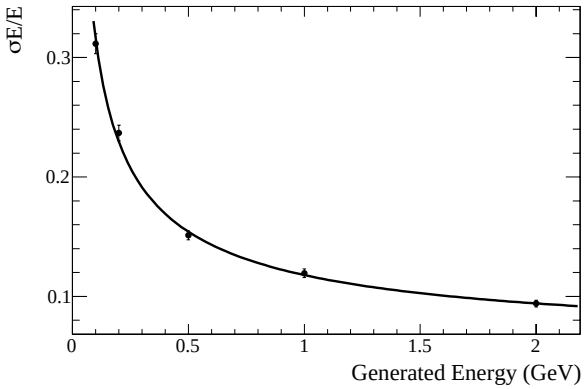

Figure 9.58: The backward EMC energy resolutions, σ_E/E, where σ_E and E are the Gaussian width and mean in Fig. 9.57, as a function of generated photon energy.

9.4.7 Backward simulation

Currently, only a simple backward EMC model exists in the GEANT4 simulation that models 24 layers of scintillator and lead. Each layer, however, is modeled by a complete disc without physical strip segmentations in r-ϕ. Support structure, fibers, electronics, and cables are presently ignored.

In the fast simulation, the model does not separate lead from scintillator. It uses instead an artificial material that approximates the overall density, radiation length, interaction length and Moliere radius of the mixture of lead and plastic. The volume is divided into eight rings, each of which is divided into 60 segments. The logarithmic spirals and the lead-scintillator layers, however, are not modeled explicitly to avoid a complicated shower reconstruction and the modeling of longitudinal shower energy distribution. The energy resolution is set to $\sigma_E/E = \frac{14\%}{\sqrt{E(\text{ GeV})}} \oplus 3\%$.

9.4.8 Performance in simulations

A GEANT4 simulation is performed to study the energy resolution under the simplified conditions, ignoring the rest of the detector and shooting mono-energetic photons perpendicular to the face of the disc. All energy deposited in the scintillator is collected. No clustering algorithm is performed. Figure 9.57 shows the energy deposition for five different photons energies, 0.1, GeV 0.2 GeV, 0.5 GeV, 1 GeV, and 2 GeV. For 0.1 GeV photons, approximately 9.5% of the photon energy is deposited in the scintillator on average. This percentage drops to 9.0% for 2 GeV photons.

The energy dependence of the energy resolutions on generated energy is shown in Fig. 9.58. The distribution can be fitted with the function $\sigma_E/E = \frac{10\%}{E(\text{ GeV})^{0.485}} \oplus 6\%$.

9.4.9 Impact on physics results

Fast simulation studies have been conducted to investigate the performance gain achieved by the addition of the backward calorimeter. The channels chosen to evaluate the impact of this detector are $B \to \tau\nu$ and $B \to K^{(*)}\nu\bar{\nu}$, since first both are benchmark channels for the Super$B$ physics program and second the detector hermeticity increases improving signal reconstruction efficiencies and background rejection.

The study of the leptonic decay $B \to \tau\nu$ is of particular interest as a test of the Standard Model (SM) and a probe for New Physics [2, 3]. The presence of a charged Higgs boson (in *e.g.*, a Two Higgs Doublet Model) as a decay mediator could significantly enhance the branching ratio above the SM value[4]. A detailed analysis of this channel is therefore quite important in searches for physics beyond the SM. A complementary search for physics beyond the SM can be performed using $B \to K^{(*)}\nu\bar{\nu}$ decays [3]. Being mediated by a flavor-changing neutral current, these processes are prohibited at tree level in the SM and the higher order diagrams may receive contribution from non-standard mechanism. Moreover, new sources of missing energy may replace the neutrinos in the final state.

The reconstruction of both decay modes is challenging, since the final state contains more than one neutrino and thus is only partially reconstructible. Signal events are selected using a recoil method analysis, in which the signal B-meson (B_{sig}) is identified as the system recoiling against the other tag B meson (B_{reco}). The tag B meson is either reconstructed fully via its hadronic decays [5], or partially reconstructed from its semileptonic $B \to D^0\mu\nu_\mu, D^0 \to K\pi$ decays [6]. The rest of the event is assigned to the $B \to \tau\nu$ candidate, and must be compatible with one of the following decay modes of the tau lepton: $\mu\nu_\mu\nu_\tau$, $e\nu_e\nu_\tau$, $\pi\nu_\tau$, $\pi\pi^0\nu_\tau$, $\pi\pi^0\pi^0\nu_\tau$, $\pi\pi\pi\nu_\tau$, $\pi\pi\pi\pi^0\nu_\tau$. These final states cover about 95% of all τ decays, and have one charged particle (1-prong) or three charged particles (3-prong), with the possible addition of one or two π^0s. Since final states containing one or more π^0 cover about 40% of the tau decay modes, an increase in the EMC coverage improves substantially the efficiency of tau identification.

Candidates for the $B \to K^{(*)}\nu\bar{\nu}$ sample have to be compatible with one of the following final states: $K^{*+} \to K_S(\pi^+\pi^-)\pi^+$, $K^+\pi^0$, $K^{*0} \to K^+\pi^-$, K^+, $K_S \to \pi^+\pi^-$ (semileptonic analysis only). In the analyses with a $K^{(*)}$ in the final state, further selection criteria are applied using kinematic quantities related to the goodness of the B_{reco} and $K^{(*)}$ reconstruction and event shape variables that test the energy balancing in the event and the presence of missing energy due to the neutrinos in the final state. The present level of the analyses is very similar to that in Refs. [**?**] and [**?**].

A large background arises from B-meson decays with undetected or misidentified particles, such as $B \to \pi^0\ell\nu$ or $B \to \eta\ell\nu$. These backgrounds are further rejected using, E_{extra}, the total neutral energy in the calorimeter of particles not associated with either B-meson. Signal events peak at low values of E_{extra}, while background events which contain additional sources of neutral showers tend to have higher values

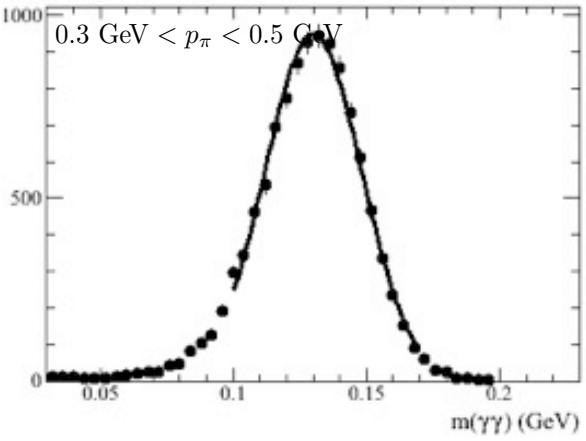

Figure 9.61: Invariant-mass resolution of $\pi^0 \to \gamma\gamma$, where one photon is detected in the backward EMC.

of E_{extra}. The discriminating power of this observable obviously increases with the calorimeter coverage. The signal and background levels are finally extracted by fitting the beam-energy substituted mass $m_{ES} = \sqrt{s/4 - p_B^2}$ distribution of the tag B-mesons.

The performance of the backward EMC is assessed by comparing the signal-to-background ratio, S/B, and the statistical precision, $S/\sqrt{S+B}$, of the expected signal with and without the backward EMC. For this task, the extra neutral energy reconstruction is split into two disjoint calorimeter regions: E^{extra}_{brrfwd} covering the barrel and the forward region and E^{extra}_{bwd} covering the backward region only. Furthermore, the effects of machine background (see section**??**) superimposed on physics events are taken into account.

The results for both rare decay channels are summarized in Table 9.6. For $B \to \tau\nu$ reconstructed in hadronic tags, the improvements in $S/\sqrt{S+B}$ are shown as a range sampling over the individual τ final states. For $B \to \tau\nu$ reconstructed in semileptonic tags, the improvement in $S/\sqrt{S+B}$ is presented as an average over all τ final states. Combining $S/\sqrt{S+B}$ of both tags, the net gain is of the order of 10%. For $B \to K^*\nu\bar{\nu}$, the net gain for hadronic and semileptonic tags combined ranges between 8% and 16% depending on the final state. For $B \to K\nu\bar{\nu}$ the net gain is about 6%.

These improvements in turn yield improvements in the precision of measured physical observables. For example, Figure 9.59 shows the expected precision of the measured $B \to K^+\nu\bar{\nu}$ and $B \to K^*\nu\bar{\nu}$ branching fractions as a function of integrated luminosity. The yellow band represents the SM prediction [2]. The red dots with red error bars are obtained from an extrapolation of *BABAR*measurements, which take into account the improvements due to the lower boost, which corresponds to a higher detector hermeticity. Dots with black error bars are obtained from the same procedure but in addition include the backward EMC. For $\mathcal{B}(B \to K^+\nu\bar{\nu})$ and $\mathcal{B}(B \to K^*\nu\bar{\nu})$ the 3 σ significance for evidence without the backward EMC is reached at 5 ab^{-1} and 51 ab^{-1}, respectively. When adding the backward EMC, the 3 σ significance is already reached at 4.5 ab^{-1} and 42 ab^{-1}, respectively.

In addition to the measurement of neutral clusters, the backward EMC can be used to improve the π^0 reconstruction efficiency. If one photon is reconstructed in the backward EMC, the $\gamma\gamma$ invariant-mass resolution improves from $\sim 24\,\mathrm{MeV}$ for $200\,\mathrm{MeV}/c$ π^0s tot $\sim 13\,\mathrm{MeV}$ for $1\,\mathrm{GeV}/c$ π^0s (see, e.g., Fig. 9.61).

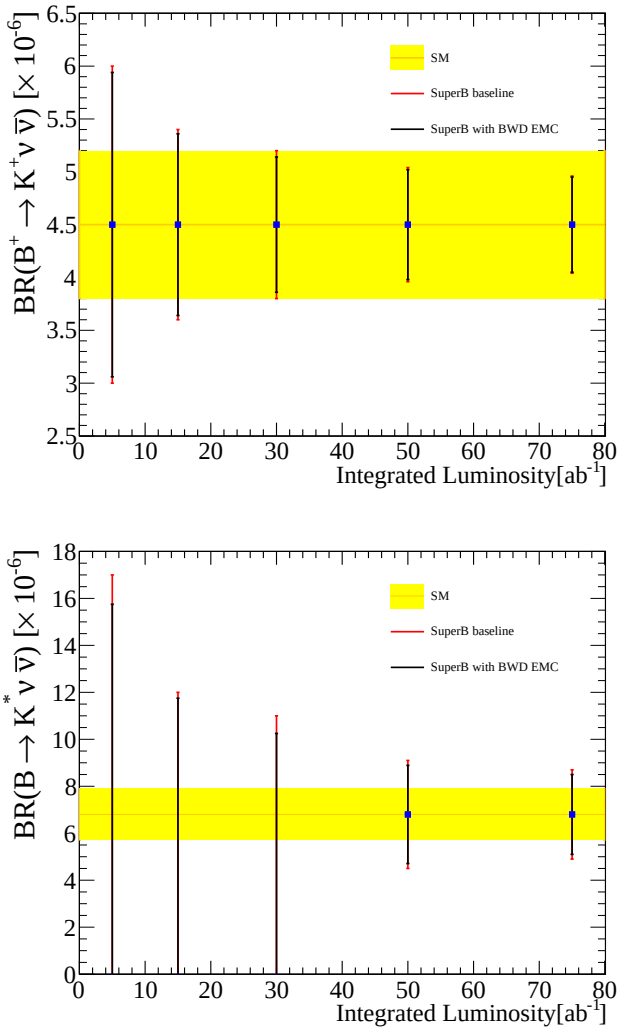

Figure 9.59: Expected precision on branching fraction measurements of (left) $\mathcal{B}(B \to K^+\nu\bar{\nu})$ and (right) $\mathcal{B}(B \to K^*\nu\bar{\nu})$ as a function of integrated luminosity. The yellow band represent the SM prediction, the black (red) error bars represent the upper limits or the branching fraction measurements with (without) the backward EMC.

Table 9.6: Relative gain in $S/\sqrt{S+B}$ by including the backward EMC in the event selection for $B \to K^{(*)}\nu\bar{\nu}$ and $B \to \tau\nu$ decay channels reconstructed in the recoil of B semileptonic and hadronic tags.The first uncertainty is statistical and the second is systematic.

channel	Semileptonic	Hadronic
$B \to \tau\nu$	$(6.1 \pm 0.1 - 0.7)\%$	$\simeq 3 - 5\%$
$B \to K^+\nu\bar{\nu}$	$(5.8 \pm 1.0 - 0.6)\%$	-
$B \to K_S\nu\bar{\nu}$	$(6.0 \pm 0.4 - 0.6)\%$	-
$B \to K^{*+}(K^+\pi^0)\nu\bar{\nu}$	$(7.0 \pm 0.2 - 0.7)\%$	$(5.9 \pm 2.5 - 0.5)\%$
$B \to K^{*+}(K_S\pi^+)\nu\bar{\nu}$		$(6.2 \pm 2.1 - 0.5)\%$
$B \to K^{*0}\nu\bar{\nu}$	$(9.1 \pm 0.4 - 0.7)\%$	$(7.3 \pm 1.8 - 0.5)\%$

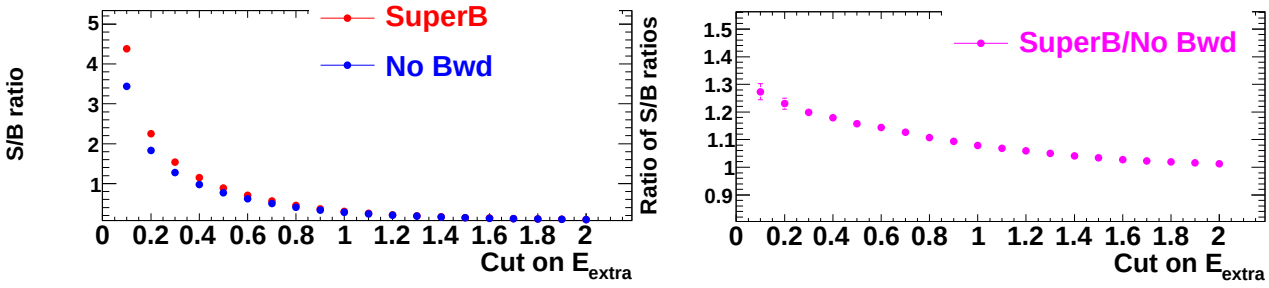

Figure 9.60: Left: Signal-to-background ratio with and without a backward EMC, as a function of the $E_{\rm extra}$ selection. Right: Ratio of the S/B ratio with a backward EMC to the S/B ratio without a backward calorimeter, as a function of the $E_{\rm extra}$ selection.

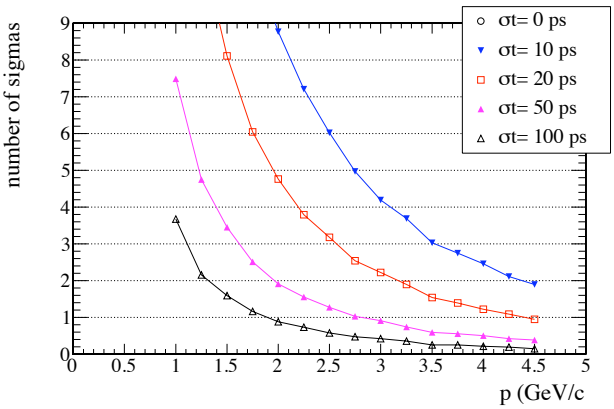

Figure 9.63: K/π separation versus measured momentum for different timing resolutions in the backward EMC. The finite separation for perfect timing is caused by uncertainties in the momentum measurement.

It is worth mentioning that the inclusion of the backward EMC not only improves the background rejection, but also the B-tagging efficiency. The impact on the B reconstruction efficiency is determined by using the decays $B^- \to D^0\pi^-, D^0 \to K^-\pi^+\pi^0$. Events are separated into two groups: the first uses only photons from the barrel and forward endcap, while the second includes photons from the backward EMC with polar angle between $-0.96 < \cos\theta < -0.89$ as well. The π^0 mass window is defined as 120–145 MeV (100–180 MeV) for the first (second) group. For B candidates, D^0 s are selected by $1.830 < m_{K\pi\pi^0} < 1.880$ GeV and $-80 < \Delta E < 50$ GeV. The $m_{\rm ES}$ distribution is fitted to determine the B reconstruction efficiency. Including the backward EMC, the signal efficiency increases by nearly 4% in this particular channel (see Fig. 9.62).

9.4.10 Use for particle identification

Charged particles moving in the backward direction typically have lower momentum. Thus, ionization loss and time-of-flight measurements may provide useful information for particle identification, *e.g.* for e/π and K/π separation.

A preliminary time-of-flight study is performed with fast simulation. Single kaons or pions are generated that move towards the backward EMC. The true arrival time calculated at the first layer is smeared with a Gaussian resolution to simulate the measured time distribution. Velocity distributions are obtained for kaons and pions at a given momentum from the measured time and reconstructed track path length. Both mean and RMS values are extracted from these distributions to determine K/π separation in units of σ as a function of momentum for different time resolutions, in which uncertainties in the momentum measurement and path length reconstruction are included. Fig. 9.63 shows K/π separation in units of standard deviations as a function of momentum for time resolutions of 100 ps, 50 ps, 20 ps, 10 ps and perfect timing. For example for 100 ps time resolution, aK/π separation of more than three standard deviations (σ) can be achieved for momenta up to 1 GeV/c and approximately 1.5σ up to 1.5 GeV/c.

Since each layer measures the time distribution, 24 measurements will be averaged. In addition to timing, the ionization is measured in each layer. For MIP-like particles, the average energy loss per layer is $dE_{Pb} = 4.3$ MeV and $dE_{scintillator} = 0.6$ MeV. A 0.5 GeV/c π is at the ionization minimum, a 0.5 GeV/c K is below the minimum and a 0.5 GeV/c e is at the relativistic plateau. For MIP particles, the ionization loss in the 24 layers is $DeltaE =$

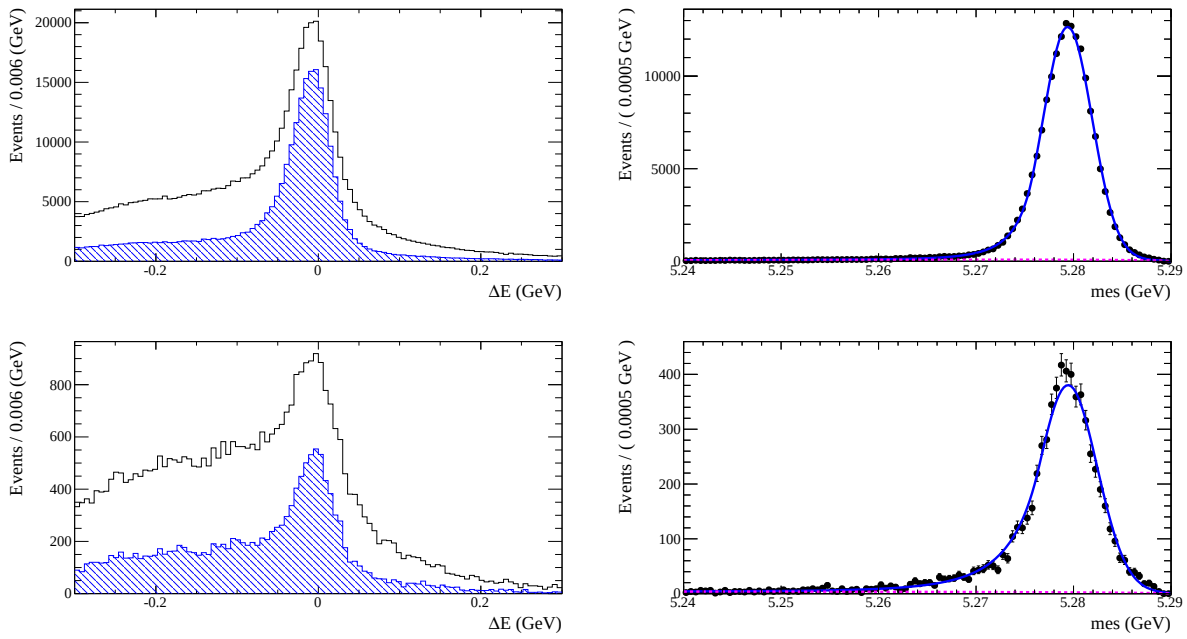

Figure 9.62: (left) ΔE and (right) $m_{\rm ES}$ distributions for the decay $B^- \to D^0\pi^-$ with $D^0 \to K^-\pi^+\pi^0$ reconstruction for (top) both γ's in barrel and forward endcap and (bottom) one γ in the backward EMC. The two histograms in each ΔE distribution are before and after a requirement on the D^0 mass.

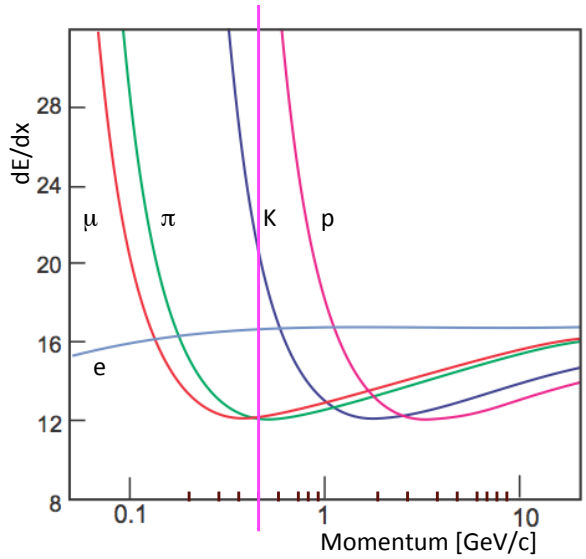

Figure 9.64: Calculated energy loss curves versus momentum for e, μ, π, K and p in one layer of the backward EMC.

117 MeV. Since the energy loss below the minimum increases with decreasing momenta as $1/\beta^2$, dE/dx measurements in the endcap can be combined with the dE/dx information from the SVT and DCH. Figure 9.64 shows the ionization curves for e, μ, π, K and p as a function of momentum. A $> 3\ \sigma$ K/π separation is achievable for momenta up to $0.6 - 0.7\,\mathrm{GeV}$.

9.4.11 Discussion of task force conclusions

In the process of deciding how to proceed with the backward EMC, a task force was convened to evaluate its various benefits and impacts. A number of conclusions came out of this:

- The device adds to the physics program in important channels through the increased hermeticity.
- The design is technically plausible and cost-effective, however: operation of the readout in the radiation environment should be studied further; a prototype should be demonstrated in a beam test.
- The possibility of using the backward EMC for PID through time-of-flight is attractive and should be pursued with further R&D.
- The capability to install this device should be preserved, as opposed to, for example, extending the drift chamber.

Bibliography

[1] C. Adloff *et al.* [CALICE collaboration] "Construction and Commissioning of the CALICE Analog Hadron Calorimeter Prototype," JINST 5:P05004 (2010).

[2] W. -S. Hou, "Enhanced charged Higgs boson effects in $B^- \to \tau\bar{\nu}$, μ $bar\nu$ and $b \to \tau\bar{\nu} + X$," Phys. Rev. D **48** (1993) 2342-2344.

[3] W. Altmannshofer, A. J. Buras, D. M. Straub, M. Wick, "New strategies for New Physics search in $B \to K^*\nu\overline{\nu}$, $B \to K\nu\overline{\nu}$ and $B \to X_s\nu\overline{\nu}$ decays," JHEP **0904**, 022 (2009).

[4] T. Barakat, "The "$B \to K^*\nu\bar{\nu}$ rare decay in the two-Higgs doublet model", J.Phys.G G24, 1903 (1998).

[5] B. Aubert *et al.* [BABAR Collaboration], "Search for $B \to K^*\nu\bar{\nu}$," Phys.Rev. D78, 072007 (2008).

[6] P. del Amo Sanchez *et al.* [BABAR Collaboration], "Search for the Rare Decay $B \to K\nu\bar{\nu}$," Phys. Rev. D **82**, 112002 (2010).

[7] V. Andreev *et al.*, "A high granularity scintillator hadronic-calorimeter with SiPM readout for a linear collider detector", Nucl.Instrum.Meth. A540, 368 (2005); T. Takeshita, "Development of MPPC", Pramana 69, 1079 (2007).

[8] M. Bouchel *et al.*, "SPIROC (SiPM Integrated Read-Out Chip): Dedicated very front-end electronics for an ILC prototype hadronic calorimeter with SiPM read-out", JINST 6, C01098 (2011).

[9] H. Ono *et al.*, "Beam test results of a high-granularity tile/fiber electromagnetic calorimeter", Nucl.Instrum.Meth. A600, 398-407 (2009).

[10] R. Faccini, "Results from silicon photomultiplier neutron irradiation test", proceedings of 11th ICATPP Conference on Astroparticle, Particle, Space Physics, Detectors and Medical Physics Applications, Villa Olmo, Como, Italy, 2009.

99

9.5 Trigger

This is a reminder that we need a synopsis of the EMC trigger somewhere in the EMC chapter, although the detailed description will be in the ETD chapter. It is to be determined whether this should be in a separate section or merged with the three sub-calorimeter sections.

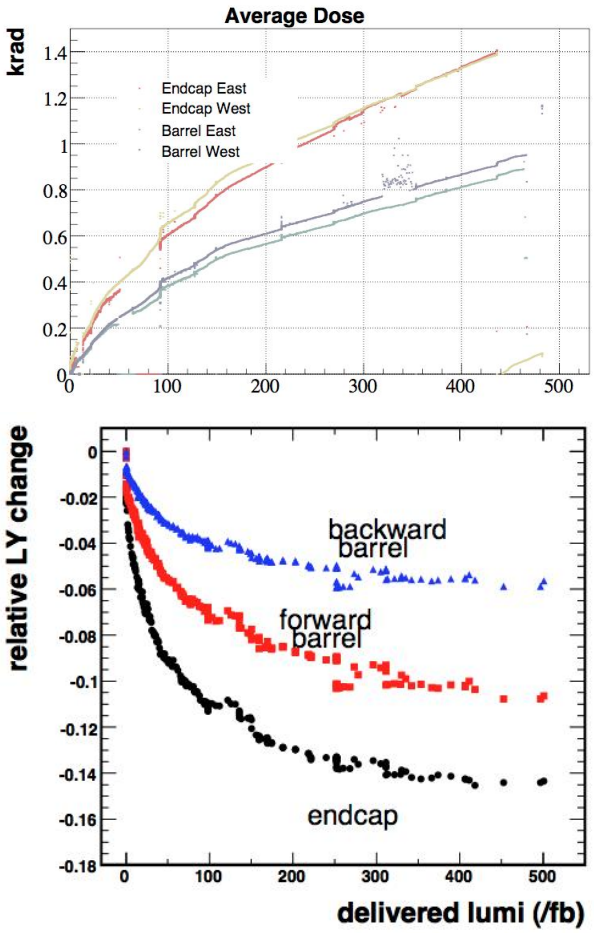

Figure 9.65: Left: Radiation dose as measured by RadFETs in the *BABAR* barrel and endcap. Right: Decrease in light output with radiation dose for the *BABAR* CsI(Tl) barrel and endcap.
These figures are placeholders; we need higher quality copies.

9.5.1 Calorimeter readout trigger

9.5.1.1 Normal mode

9.5.1.2 Calibration mode

9.5.2 Calorimeter trigger primitives

9.6 Detector protection

Personnel ES&H will be elsewhere.

9.6.1 Thermal shock

9.6.2 Mechanical shock, including earthquakes

9.6.3 Fluid spills

9.6.4 Electrical surges, outages

9.6.5 Radiation damage

Radiation exposure from Bhabha, Touschek and beam-gas scattering is monitored by a set of 56 realtime integrating dosimeters (Rad-FETs) placed in front of the barrel and 60 RadFETs in front of the endcap. The accumulated dose, measured by these RadFETs over the life of the *BABAR* detector, along with the observed loss in scintillation light output is shown in Figure[**?**], separately for the endcap, the forward, and the backward barrel of the calorimeter. The dose over the life of Super$B$ is expected to be two orders of magnitude greater.

9.7 Cost & Schedule

This will appear elsewhere.

9.7.1 WBS structure

9.7.2 Gantt chart

9.7.3 Basis of estimates

9.7.4 Cost and schedule risks

Bibliography

[1] The EMC bibliography items should be placed in the file `EMC/EMC-bibliography.tex`.